Mapping variations in bedrock weathering with slope aspect under a sedimentary ridge-valley system using near-surface geophysics and drilling

Berit Hudson-Rasmussen[1], Mong-Han Huang[1], W. Jesse Hahm[2], Daniella Rempe[3], David N Dralle[4], and Mariel D Nelson[5]

[1]University of Maryland, College Park
[2]Simon Fraser University
[3]University of Texas at Austinn
[4]Pacific Southwest Research Station, United States Forest Service
[5]University of Texas at Austin

November 25, 2022

Abstract

Understanding how soil thickness and bedrock weathering vary across ridge and valley topography is needed to constrain the flowpaths of water and sediment within a landscape. Here, we investigate how soil and weathered bedrock properties vary across a ridge-valley system in the Northern California Coast Ranges where topography varies with slope aspect such that north facing slopes, which are more densely vegetated, are steeper. In this study, we use seismic refraction surveys to extend observations made in boreholes and soil pits to the hillslope scale and identify that while soils are thicker on north facing slopes, the thickness of weathered bedrock does not vary with slope aspect. We estimate the porosity of the weathered bedrock and find that it is several times the annual rainfall, indicating that water storage is not limited by the available pore space, but rather the amount of precipitation delivered. Bedding-parallel and bedding-perpendicular seismic refraction surveys reveal weathering profiles that are thickest upslope and taper downslope to channels. We do not find a clear linear scaling relationship between depth to bedrock and hillslope length, which may be due to local variation in incision rate or bedrock hydraulic conductivity. Together, these findings, which suggest that the aspect-independent weathering profile structure is a legacy of past climate and vegetation conditions and that weathering varies strongly with hillslope position, have implications for hydrologic processes across this landscape.

Mapping variations in bedrock weathering with slope aspect under a sedimentary ridge-valley system using near-surface geophysics and drilling

Berit M. Hudson Rasmussen[1], Mong-Han Huang[1], W. Jesse Hahm[2], Daniella M. Rempe[3], David Dralle[4] and Mariel D. Nelson[3]

[1]Department of Geology, University of Maryland, College Park, MD, USA,
[2]Department of Geography, Simon Fraser University, Burnaby, BC, Canada,
[3]Department of Geosciences, Jackson School of Geosciences, The University of Texas at Austin, Austin, TX, USA,
[4]Pacific Southwest Research Station, United States Forest Service, Albany, CA, US

Plain Language Summary

Below Earth's ground surface, porous space within weathered bedrock can store a significant amount of water, which is essential for our ecosystem. Collecting hydrologic data and core samplings from boreholes provide direct measurements about how material weakens towards the ground surface due to weathering. It also provides an estimate of moisture in the subsurface that is available for trees to consume during dry summers. Our study site is located in a series of ridges and valleys in northern California, USA, where it has distinctive dry summers and wet winters. This site represents a common topography along the east side of the Coastal Range. Besides borehole and hydrologic data, we conduct complementary seismic refraction surveys to image material strength in 2D. 2D images can better capture the lateral variation of weathering zone thickness from channels to ridgetops, and we can infer moisture distribution by combining borehole and seismic refraction. The results show a rapid increase of material strength that agrees with borehole observations. Although vegetation density is very different between the north and south facing hills, the depth to fresh bedrock is roughly the same. We also find that the ridges here can store a lot more water than annual precipitation.

Abstract

Understanding how soil thickness and bedrock weathering vary across ridge and valley topography is needed to constrain the flowpaths of water and sediment within a landscape. Here, we investigate how soil and weathered bedrock properties vary across a ridge-valley system in the Northern California Coast Ranges where topography varies with slope aspect such that north facing slopes, which are more densely vegetated, are steeper. In this study, we use seismic refraction surveys to extend observations made in boreholes and soil pits to the hillslope scale and identify that while soils are thicker on north facing slopes, the thickness of weathered bedrock does not vary with slope aspect. We estimate the porosity of the weathered bedrock and find that it is several times the annual rainfall, indicating that water storage is not limited by the available pore space, but rather the amount of precipitation delivered. Bedding-parallel and bedding-perpendicular seismic refraction surveys reveal weathering profiles that are thickest upslope and taper downslope to channels. We do not find a clear linear scaling relationship between depth to bedrock and hillslope length, which may be due to local variation of incision rate or bedrock hydraulic conductivity. Together, these findings, which suggest that the aspect-independent weathering profile structure is a legacy of past climate and vegetation conditions, and that weathering varies strongly with hillslope position, have implications for hydrologic processes across this landscape.

Key points

1. Depth of fracturing and chemical alteration is greatest on ridges and thinnest along channels.
2. Despite a strong aspect dependent contrast in soil thickness, weathering thickness does not vary with slope aspect.
3. Water storage in weathered bedrock is limited by rainfall instead of porosity available for water storage.

1. INTRODUCTION

The transformation of fresh bedrock into mobile soil in the critical zone (CZ) is facilitated by changes in chemical composition, material strength, and porosity with depth. These processes dictate how landscapes store and release water to trees and streams (Brooks et al., 2015). Documenting the structure of the CZ, including the thickness and subsurface topography of different materials, is therefore crucial to quantifying water storage (Rempe & Dietrich, 2014; Flinchum et al., 2018a; Callahan et al., 2020) and predicting ecosystem and landscape response to climate change (Godderis and Brantley, 2013; Sullivan et al., 2022). Water storage dynamics are not homogenous at the hillslope scale, but are influenced by microtopography (Wang et al., 2021), elevation (Klos et al., 2017; Nielsen et al., 2021), and slope aspect (Anderson et al., 2014). CZ structure can additionally be modulated by lithology (Hahm et al., 2014; Leone et al., 2020) and climate (Inbar et al., 2018; Anderson et al., 2019). Exploration of the spatially variable hydrologic dynamics of a landscape therefore requires characterization of CZ structure over broad spatial scales, and in different geologic settings.

Many studies have observed that with increased solar radiation on equator-facing hillslopes at mid-high latitudes, separate microclimates can be found on equator-facing (south-facing, in California) versus pole-facing (north-facing) hillslopes (Pelletier et al., 2018). In presently precipitation-limited environments (as opposed to temperature-limited), north-facing slopes of the northern hemisphere tend to have more vegetation, and thicker, wetter soils, while south-facing slopes are dryer, and less vegetated with thinner soils (Pelletier et al., 2018). While surface slope, tree density, and soil thickness have been well documented to vary based on aspect dependency (Bale et al., 1998; Inbar et al., 2018), fewer studies address the influence of aspect dependency and climate on deeper weathering transitions.

Seismic refraction can effectively capture the heterogeneity in the subsurface weathered bedrock structure, which can vary drastically from ridge to channel (Leone et al., 2020; Wang et al., 2021). By combining borehole and geophysical methods, recent studies have calibrated geophysical data to direct observations to infer weathering thickness across a landscape (Holbrook et al., 2014, 2019; Flinchum et al., 2018a; Hayes et al., 2019; Gu et al., 2020). This combined approach allows for better modeling of subsurface water flow dynamics (Gu et al., 2020), comparison of slope aspect microclimates (Leone et al., 2020), and rock physics modeling of porosity (Holbrook et al., 2014; Hayes et al., 2019; Callahan et al., 2020; Gu et al., 2020; Grana et al., 2022). These studies are important advances and have helped to test and calibrate models of CZ evolution, but they have documented only a fraction of the diverse combinations of topography, biota, lithology, and climate present across Earth's terrestrial surface.

In this study, we image CZ structure through active-source seismic refraction surveys across a series of sedimentary ridges and valleys in the Mediterranean climate of the California Coast Ranges, USA. Characterizing water storage dynamics in this setting is essential as this landscape faces increased drought frequency (East and Sankey, 2020) and rainfall-triggered landslides (Nelson et al., 2017; Sanders et al., 2019; Handwerger et al., 2019). A 2018 drilling campaign established weathered material extending 11-17 m below ridgetops, and only 1-2 m below channels. Building on this previous work, we ask: 1) How does weathering, as expressed by bedrock fracturing and chemical alteration, vary with hillslope aspect? 2) What is the role of sedimentary bedding orientation in CZ structure? 3) What is the water storage capacity of the weathered bedrock and how does this vary across the landscape? To respond to these questions, we perform a comprehensive comparison of seismic velocity with physical, chemical, and hydrologic properties measured through borehole analysis by Pedrazas et al (2021).

2. FIELD SITE

2.1 Geologic Setting

The study site, Rancho Venada (RV), is located 16 km west of Williams, California, USA, on the western border of the Sacramento Valley, and is lined with 100 m relief hills organized parallel to the strike of east-dipping turbidite beds (**Figure 1**). We focus on a ridge dissected by evenly spaced (~100-150 m) channels. The specific hills included in this study—referred to as MH2R, MH3R, and MH7R—are underlain by late Cretaceous bedrock of the Great Valley Sequence, composed primarily of thinly interbedded mudstone and siltstone, and capped with sandstone (**Figure 1**; Rich, 1971; Pedrazas et al., 2021). These units are separated from the deformed metamorphic Franciscan Complex by the Stony Creek Fault Zone to the west (Rich, 1971). Originally uplifted and tilted due to the subduction of the Farallon Plate below the North American Plate, RV has been experiencing general northwest-southeast compression for the past 3-5 Ma (Atwater and Stock, 1998). There are no major faults or folds within these ridges, with only cm-to-meter-scale structures (monocline fold) observed (Harwood and Helley, 1987; Rich, 1971). The hills were formed at least ~1-2 Ma based on a channel incision rate of ~0.1 mm/yr (Pedrazas, et al., 2021). The regional climate is semi-arid with pronounced wet and dry seasons and a mean precipitation of 534 mm/yr (Hahm et al., 2022). Vegetation is primarily grassland and oak woodland, with a notable lack of trees on south-facing hillslopes and a higher vegetation density on the north-facing hillslopes (see **Figure 1b,c**).

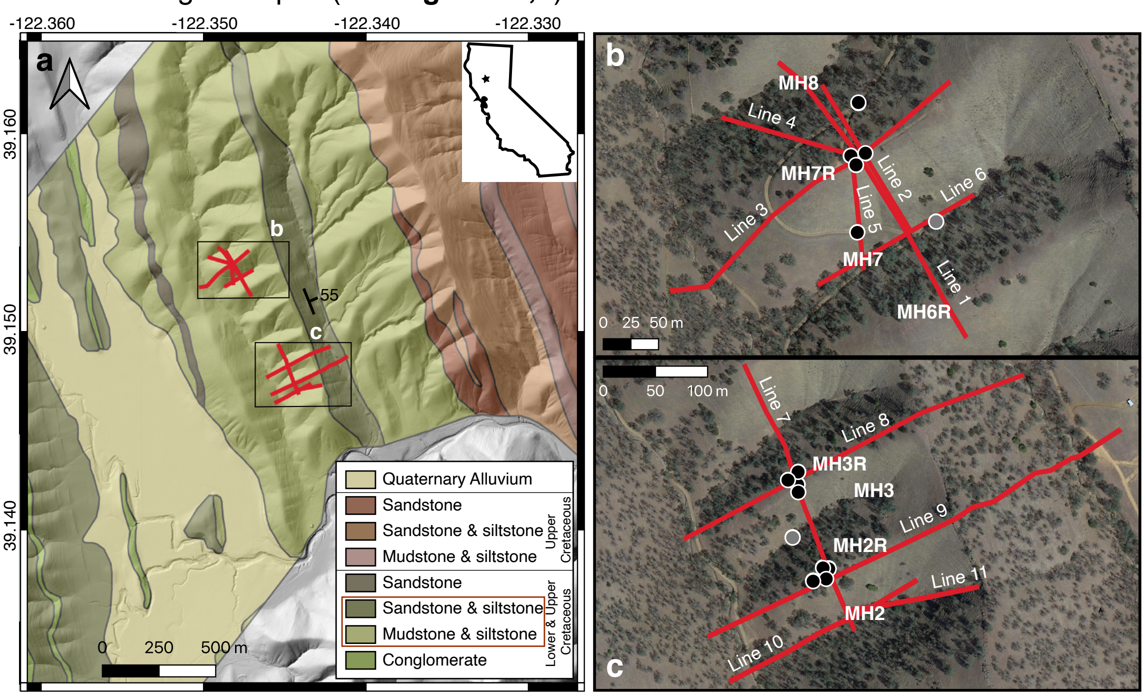

Figure 1. Geologic map of the study location near Williams, California, USA (after Rich, 1971 and Nelson et al., 2017). The black star in the inset map indicates the study site Rancho Venada (RV). Inset **b** and **c** show the locations of the specific hills of interest and the contrasting tree density on north and south-facing

slopes. Red lines represent seismic survey lines 1-10. Black circles indicate locations of boreholes cored using a drill-rig, while gray circles were drilled using a Shaw backpack drill (Pedrazas et al., 2021).

2.2 Previous Studies

Fourteen boreholes were drilled along three hills at RV in November, 2018 (Pedrazas et al., 2021). Three deep boreholes were drilled to the total relief of the hills: 47, 20, and 20 m for MH7R, MH3R, and MH2R, respectively. The drilling process involved augering, coring, and standard penetration tests to obtain blowcount rate (Pedrazas et al., 2021). Shallower boreholes were augered to 6-9 m depth or drilled with a Shaw rig to < 2 m in the channels. All boreholes were sampled for elemental composition and density, and images were produced using an optical borehole imager (OBI) for each of the three deep boreholes to capture color as well as fracture and bedding density and orientation. Neutron count measurements were taken every foot by lowering the probe down each borehole until right above the water table. These measurments were repeated every month over the course of 2 years to measure the relative seasonal water storage with depth (**Figure 2c-f**). Drilling logistics and borehole measurements are described in detail in Pedrazas et al. (2021).

Borehole analysis highlighted three interfaces across RV hillslopes: *Interface 1* as the soil - pervasively fractured material transition (i.e. soil to saprolite), *Interface 2* as the pervasively fractured - discretely fractured rock transition (i.e. saprolite to weathered bedrock), and *Interface 3* as the discretely - rarely fractured rock transition (i.e. weathered to fractured bedrock). τ analysis, tracking chemical changes as the parent material is weathered, indicates depletion of magnesium, sodium, and potassium towards the surface (**Figure 2a**). The pyrite oxidation front is also observed at a 6 - 7 m depth for all boreholes (**Figure 2a**). Matrix porosity for all sites ranges from 15-20% near the surface and drops to 10% within 5 m, and even lower to 5% by 24 m (**Figure 2b**). The MH3R and MH7R ridges display a large jump in blowcount rate, indicating increase in material strength, at a 6-7 m depth (**Figure 2d**), while MH2R shows a more gradual increase in blowcount rate. Neutron probe counts indicate dynamic seasonal rock moisture storage to a depth of 8-9 m (**Figure 2c**). Pedrazas et al. (2021) therefore propose the Interface 2 (saprolite-weathered bedrock) transition depths (MH7R: 6.5 ± 0.8 m, MH3R: 6.3 ± 0.8 m, MH2R: 7.5 ± 1.6 m; Pedrazas et al., 2021) based on the sharp increase in blowcount rate and the pyrite weathering front observed in each borehole. The saprolite above Interface 2 shows depletion of Mg, Na, and K, higher porosity, substantial fracturing, and storage of seasonally variable rock moisture. Yellowness hue, an indicator of chemical weathering, drops abruptly at a 17.5, 11, and 10.5 m depth for MH7R, MH3R, and MH2R, respectively. Pedrazas et al. (2021) define the Interface 3 (weathered- fractured bedrock) transition at the above depths based on yellowness hue and further decrease in fracture density.

Hydrologic analysis by Hahm et al. (2022) utilized a combination of remotely sensed soil moisture and evapotranspiration data, water level and downhole rock moisture surveys, and oak sapflow and water potential measurements to monitor seasonal water storage and vegetation dynamics at RV. During two drought years, the winter wet season did not replenish the subsurface storage capacity enough to recharge groundwater, discharge water as streamflow, or sustain trees, which exhibited lower sapflow and smaller leaf size. Their results suggest that RV has a large water-holding storage capacity relative to the precipitation it receives during meteorological droughts, and is therefore precipitation-limited (in the sense of Hahm et al., 2019). Repeat downhole neutron probe measurements across the 2019-2021 water years characterized seasonal rock moisture dynamics at RV, and estimated volumetric water content to vary between 25-40% throughout the year.

Huang et al. (2021) conducted a seismic survey parallel to the bedding strike along the MH2-MH4 catchments at RV in December 2019. In this study, we examine the same seismic refraction result (section 4.1.3) in comparison with data from drilling and nine additional seismic surveys to understand the deep CZ structure.

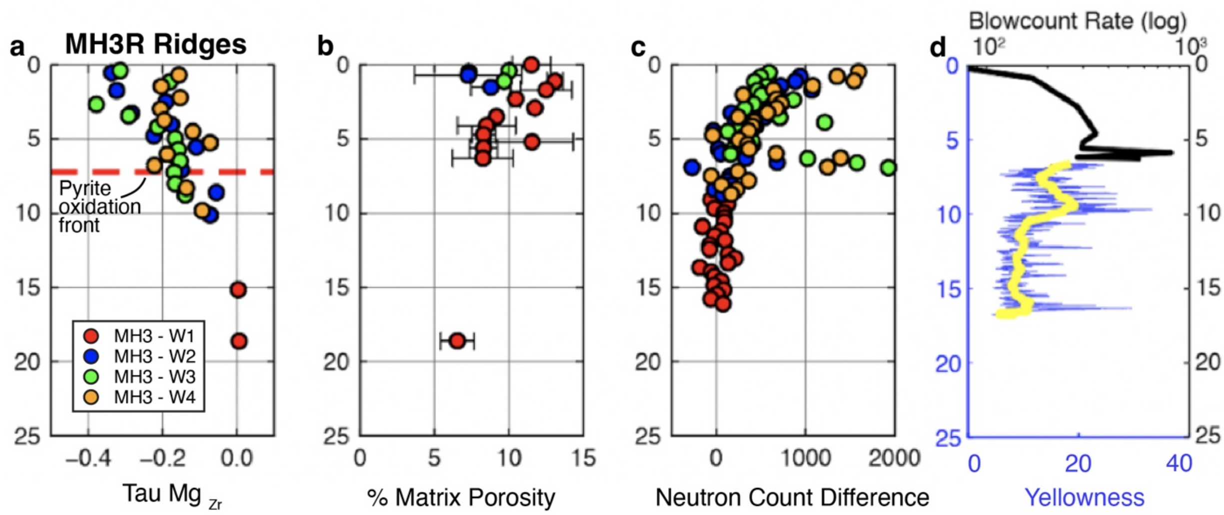

Figure 2. Borehole data for the MH3R ridgetop in Line 6 (see Figure 1 for location). Data is from Pedrazas et al. (2021). (**a**) Depletion of magnesium with depth, relative to the parent material, with zirconium as the immobile element. The pyrite oxidation depth (from sulfur) shown as the red dashed line at 6.3 m. (**b**) Matrix porosity, (**c**) neutron count difference, highlighting where moisture storage in the borehole is variable, and (**d**) log blowcount rate from a standard penetration test on the upper x-axis. Yellowness hue (blue line) is shown on the lower x-axis. The yellow line represents the smoothed yellowness hue.

3. METHODS

3.1 Seismic Refraction Surveys and Modeling

We conducted 11 active-source seismic refraction surveys at RV: three lines oriented parallel to bedding (including one previously published bedding-parallel line, Line 7; Huang et al., 2021), six perpendicular to bedding, and two along the steepest descent of the north and south-facing hillslopes (**Figure 1**). Parameters of the seismic surveys are shown in **Table S1**. We used 14-Hz geophones and created sources at a 3-10 m shot interval using 5 to 7 kg sledgehammers on a metal plate, which were recorded using the Geometrics ES-3000 system and Geoid systems. For all lines except Line 9, the shot interval was one meter near borehole locations. We performed off-end shots 36-54 m away from the first geophone and after the last geophone for each survey. Locations along the seismic line were recorded with GPS to create an elevation profile of each seismic line using a digital elevation model (DEM) generated from an airborne lidar survey of RV in 2017 (Dietrich, 2019).

We used the Geometrics PickWin software package to pick p-wave arrival times and the THB rj-MCMC inversion scheme from Huang et al. (2021) to generate seismic velocity models. For traditional inversion methods, smoothing is commonly used to regularize the inversion in order to reduce roughness coming from measurement errors. However, the smoothing parameter is normally set arbitrarily because measurement error from p-wave picking is generally unknown. The THB rj-MCMC method uses a probabilistic model to estimate measurement uncertainty (called hyperparameter) and whether measurement uncertainty propagates with source-receiver distance. THB rj-MCMC produces a posterior distribution of an ensemble of velocity models that can fit the p-wave measurements equally well, therefore we capture both the range of plausible solutions and the uncertainty associated with the model (Burdick and Lekic, 2017). The standard deviation of ensemble velocity can be calculated from the accepted models to indicate areas where the velocity has greater uncertainty (Huang et al., 2021). The THB method therefore allows for analysis of data uncertainty and explores model resolution along lateral distance and depth, which are important for assessing the reliability of seismic velocity images and interpretation of critical zone structure (**Figure 3**).

3.2 Borehole Comparison and Hillslope Analysis

To compare borehole data to seismic velocity measurements, we created a vertical velocity profile for each borehole located within 10 m of a seismic survey. We examined the p-wave velocity corresponding to the interface depth ranges from Table 1 of Pedrazas et al. (2021). Several boreholes were imaged by more than one seismic line and therefore have multiple recorded velocities. We averaged the velocity at each interface across all borehole-velocity profiles of the same survey line orientation. Since the interfaces are not abrupt boundaries, but transitional zones, we calculated the average velocity of the Interface 2 (saprolite to weathered bedrock transition) depth ± 1 standard deviation. Our result is a range of velocities over which we expect more rapid changes in material strength to occur. We then use this velocity zone to compare weathering structure across the three ridges. While borehole data at RV is limited to ridgetops and one mid-slope location, we calculate the depth to the bedding-parallel Interface 2 velocity range across the entire hillslope. We then compare the depth of this velocity range between north and south-facing hillslopes to examine aspect differences in rock weathering. To account for different lengths of hillslopes, we divide horizontal distance and depth by the hillslope length to examine normalized profiles. We do the same process for Interface 3 (weathered to fractured bedrock transition).

3.3 Porosity Modeling

Following Hayes et al. (2019), Holbrook et al. (2014), and Gu et al. (2020), we used a rock physics model to estimate bulk porosity and water saturation in the saprolite and weathered bedrock. Although most of the bedrock is sedimentary (sandstone, shale, siltstone), the detailed mineral composition at RV is not well constrained. We assumed three mineral components, quartz, feldspar, and illite, that have been mapped at RV, and varied the relative concentrations of each, with quartz: 20-50%, feldspar: 20-30%, and illite: 20-60% (Rich, 1971), to produce a range of bulk and shear moduli for the protolith. We then used the Hertz-Mindlin contact theory to calculate the dry bulk and shear modulus of the saprolite with shale or sandstone protolith, assuming a critical porosity (ϕ_c) = 0.4, contact points (n) = 10, and an empirical parameter (e) = 5 (after Gu et al., 2020). Since saturation also contributes to the bulk modulus and we do not know saturation with depth, we vary water saturation between 0-100 % and use Gasman's equation (Helgerud et al., 1999) to calculate the bulk and shear modulus of saprolite at different saturation states for each possible porosity value. With these bulk and shear moduli, we can then calculate seismic velocity using:

$$Vp = \sqrt{\frac{K_{sat} + \frac{4}{3}\mu_{sat}}{\rho_b}} \;, \tag{1}$$

where Vp, K_{sat}, μ_{sat}, and ρ_b are the seismic velocity, bulk modulus, shear modulus, and bulk density, respectively. We then compare Vp to the observed seismic velocity profile at each borehole. Since both porosity and saturation are unknown, the best-fitting velocities present a tradeoff curve between porosity and saturation, where any point along the curve can predict the same Vp.

Between volumetric water content (θ) and saturation (S), a second porosity-saturation tradeoff is created using:

$$\theta = \frac{S}{\phi} \;, \tag{2}$$

where θ is constrained from downhole repeat neutron probe measurements taken at RV within a few days of each seismic survey (Hahm et al., 2022). Using the porosity-saturation tradeoff relationship obtained from Vp and the measurement of volumetric water content, we can determine porosity and saturation.

We additionally estimated porosity assuming changes in bulk τ (i.e. mass loss due to chemical depletion) were solely responsible for porosity production, as in Hayes et al. (2019). This assumes rock weathering is dominated by chemical reactions with no contribution from physical strain. We calculated bulk τ (a measurement of chemical depletion) from concentrations of the immobile element zirconium using the formula (after Hayes et al., 2019):

$$\tau = \frac{C_{i,p}}{C_{i,w}} - 1 \;, \tag{3}$$

where τ represents the bulk mass transfer coefficient, and $C_{i,p}$ and $C_{i,w}$ represent the concentration of zirconium in the protolith and weathered material, respectively. When volumetric strain is assumed to be zero, porosity becomes -τ (Equation S13 of Hayes et al., 2019). We did not calculate volumetric strain at RV because measurements of density and zirconium concentration were not co-located.

To construct a 2D model of bulk porosity, we assumed saturation gradually increases with depth from 50-100%, based on the saturation profile constrained from the 1D model. The 2D porosity models allow us to estimate the water holding capacity by averaging porosity values at the same depth below the surface within a given horizontal range (Callahan et al., 2020). We can then integrate the porosity from the weathered bedrock depth to the surface over a 20 m wide horizontal distance at each ridgetop, where porosity is assumed to be laterally homogeneous.

4. RESULTS

4.1 Seismic velocity between ridges and channels

2D seismic images reveal changes in p-wave velocity (Vp) across the landscape. For all surveys, we mask out velocity past the ends of each line where no geophones are present. We additionally mask out regions where normalized smoothed raypath density is below 0.1 rays per model grid (using median filter with 5-pixel radius) and where coefficient of variation (CoV; standard deviation divided by mean velocity) > 30%. Low-velocity material is defined as Vp < 1000 m/s, mid-velocity as 1000 < Vp < 3000 m/s, and high-velocity as Vp > 3000 m/s. In this section, we report results of Lines 1, 6, 7, and 8. The results of Line 2-5 and Lines 9-11 can be found in the Supplementary Materials. THB rj-MCMC provides information about the overall performance of the inversion (**Figure 3**). This includes the root mean square (RMSE) misfit of the predicted p-wave arrival times of each Markov Chain in different iterations (**Figure 3a**), a noise hyperparameter that can objectively estimate data uncertainty (**Figure 3b**), a model misfit distribution of the mean velocity model with different source-receiver distance, the standard deviation of that distribution (**Figure 3c-d**), the p-wave arrival time model fitting to data of the mean velocity model (**Figure 3e**), and a normalized raypath density distribution of the mean velocity model (**Figure 3f**).

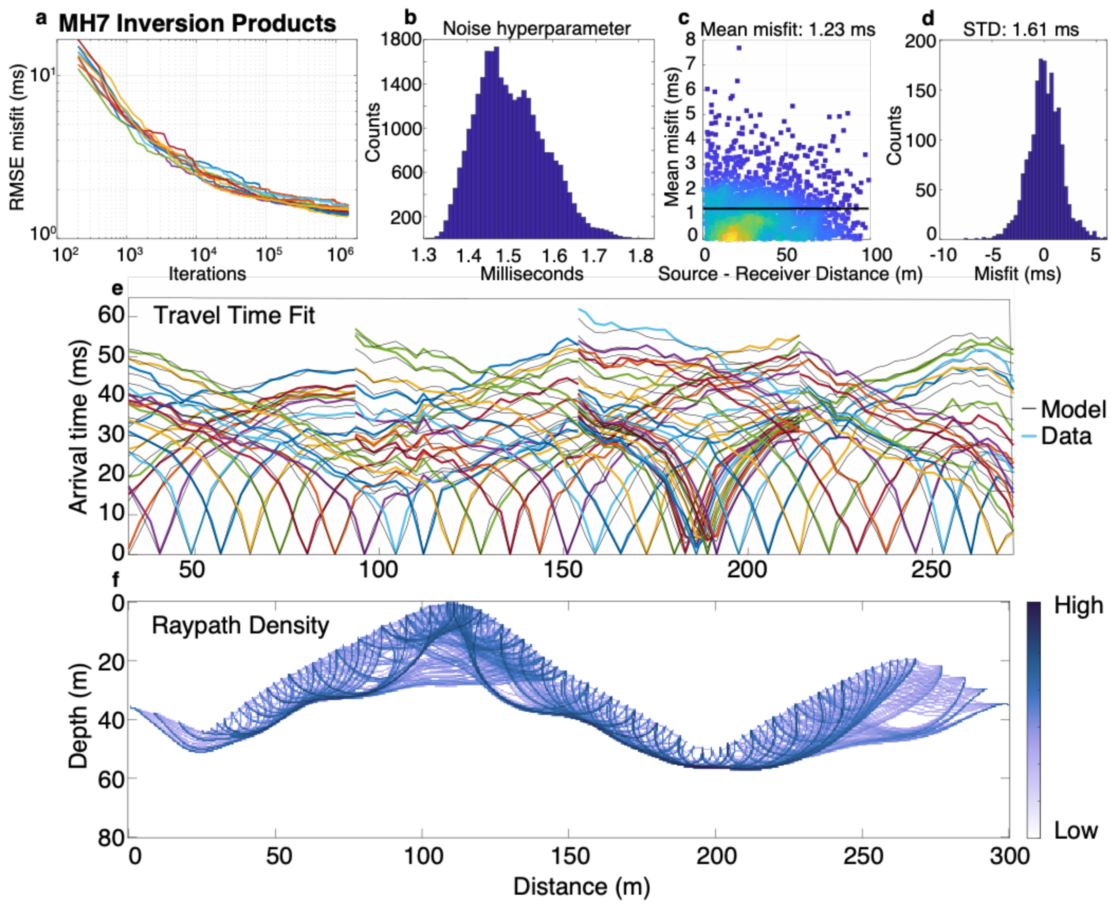

Figure 3. THB rj-MCMC products for MH7. (a) RMSE misfit evolution in log-log scale. (**b**) Noise hyperparameter distribution after burn-in. (**c**) Mean misfit with source-receiver distance of the mean velocity model. (**d**) Standard deviation of the misfit in the mean velocity model. (**e**) Modeled travel time (black lines) and observed travel time (colored lines) of the mean velocity model. (**f**) Normalized raypath density of the mean velocity model.

4.1.1 MH7R Bedding-Parallel transect (Line 1)

Below the ridgetop (MH7R), uncertainty is higher (CoV > 30%) due to low raypath density. We therefore mask out much of the region and can only resolve 10 m below the ridgetop (**Figure 3ab, Figure 4b**). Below the hillslopes, we can reliably resolve depths up to 20 m, while we can only resolve 10 m at the channels due to a rapid increase of seismic velocity. Three boreholes (MH7-W1, MH7-W2, and MH7-W3) at MH7R are within 10 m of Line 1 (**Figure 1**).

Below channels (MH7 and MH8), higher velocities are present at shallow depths, while towards the ridgetops, velocities < 3000 m/s extend for over 20 m (**Figure 4a**). The highest 2D velocity gradients occur below the channels, where velocity increases from 400 m/s to 4000 m/s within 5 meters (**Figure 4c**). A >300 m/s/m gradient contour zone can be traced across the hillslopes, suggesting a change in material strength within this high gradient zone. The 3000 m/s contour line does not mirror the surface topography at the ridgetop. However, we do not have deep enough ray paths to constrain whether Vp > 3000 m/s extend below the elevation of the channel (**Figure 4a**). A second survey line (Line 2 in **Figure 1b**) was conducted parallel to bedding across MH7R with twice as many geophones in efforts to obtain deeper ray paths and resolve velocity below the ridge (see **Figure S1**). Line 2 resolves deeper material below the hillslopes, reaching Vp > 3500 m/s above the elevation of the channel, but we were still unable to resolve structure below 14 m at the ridgetop, likely indicating a near constant seismic velocity below this depth.

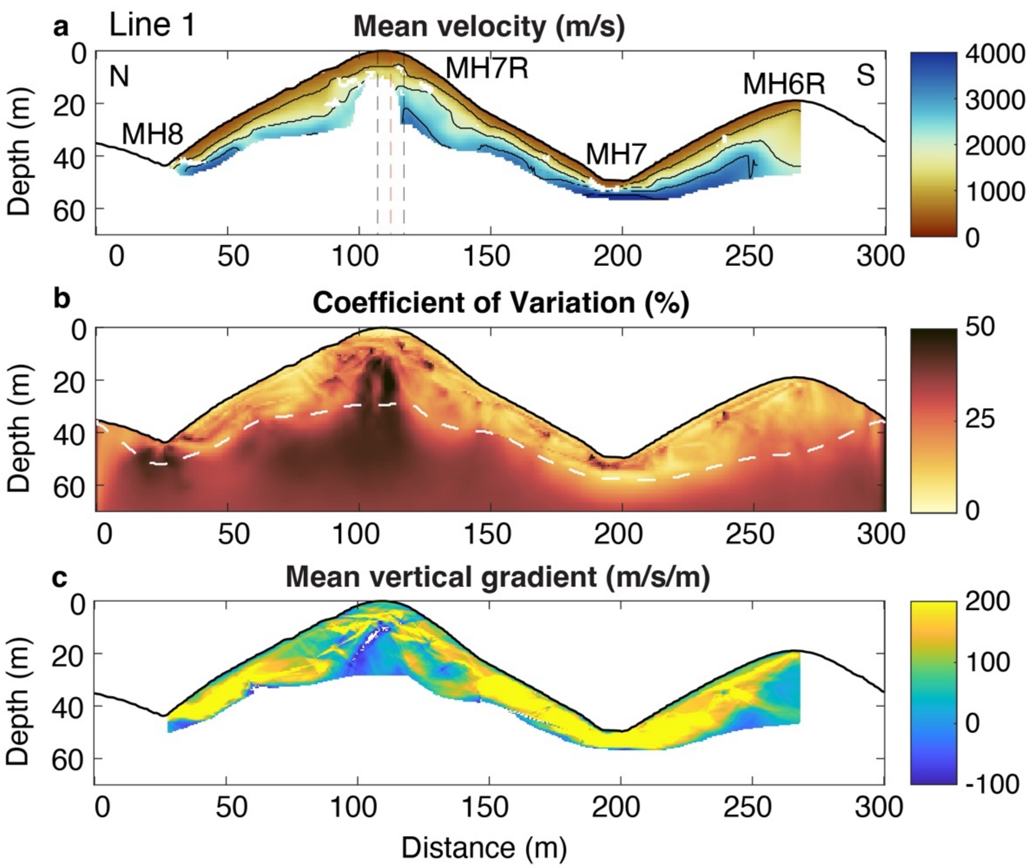

Figure 4. Results of Line 1 inversion using THB rj-MCMC (Huang et al., 2021). (**a**) Mean velocity model with contour lines at 1000, 2000, 3000, and 4000 m/s. The model is masked out where no geophones are present (edges of survey), below the deepest raypath, and where coefficient of variation (CoV; standard deviation/mean velocity x 100) > 30%. Vertical dashed lines highlight the locations of boreholes within 10 m of the survey line. From north to south, these include boreholes MH7-W2, MH7-W1, and MH7-W3 for Line 1. The orange vertical line indicates the intersection point of Lines 1 and 3. (**b**) Percent CoV with the deepest raypath as the white dashed line. (**c**) Mean vertical velocity gradient (m/s/m).

4.1.2 MH7 Channel (Line 6)

Much of the shallow velocity profile for Line 6 has low raypath density due to a high velocity contrast at shallower depth, which does not allow for deep raypaths without a longer source-receiver distance. Since weathering transitions happen at shallow (< 5 m) depth below the channel, we show an interpolated version of the mean velocity (**Figure 5a**). Vp rapidly reaches 3000 m/s within 1-5 m of the surface, with a slightly shallower high gradient zone farther east. The seismic survey configuration does not have sensitivity below ~10 m depth. Velocity for Line 6 agrees with Line 1 at their intersection (red line at 90 m). The MH2 channel (Lines 10-11) is shown in **Figure S6** and reaches high velocities within 6m of the surface on the western side, and within 2m further east.

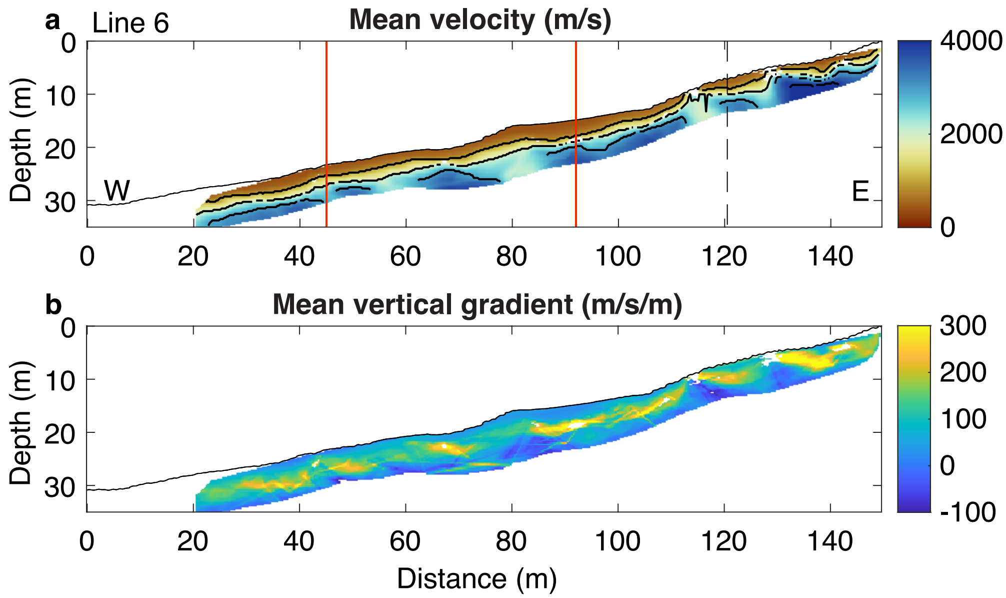

Figure 5. Results of Line 6 inversion. (**a**) Interpolated mean velocity model with contour lines at 1000, 2000, 3000, and 4000 m/s. The model is masked out below the deepest raypath and where CoV > 40%. Black dashed lines highlight the locations of boreholes within 10 m of the survey line. Red lines indicate the intersection points with Line 5 (45 m) and Line 1 (90 m). (**b**) Mean vertical velocity gradient (m/s/m).

4.1.3 MH3R and MH2R Bedding-Parallel (Line 7)

Line 7 is the same transect shown in Huang et al. (2021). Four boreholes at MH3R are within 10 m of Line 7: MH3-W1, MH3-W2, MH3-W3, and MH3-W4. Results of this survey indicated an upslope-thickening weathering profile for MH3R, with low-velocity (< 1000 m/s) material extending 5 m below the ridge and <1 m below the MH3 channel (**Figure 6a**). Three boreholes at MH2R are within 10 m of Line 7: MH3-W5, MH3-W6, and MH3-W7. The MH2R ridgetop presents a different velocity structure than its neighbor. Low-velocity material extends to a similar depth of 5-6m, but mid-velocity material extends further below the ridgetop than at MH3R. Velocities at MH2R increase gradually, remaining at 2000 m/s even at depths of 20 m below the ridge. The 3000 m/s contour is barely reached within the resolvable depth range.

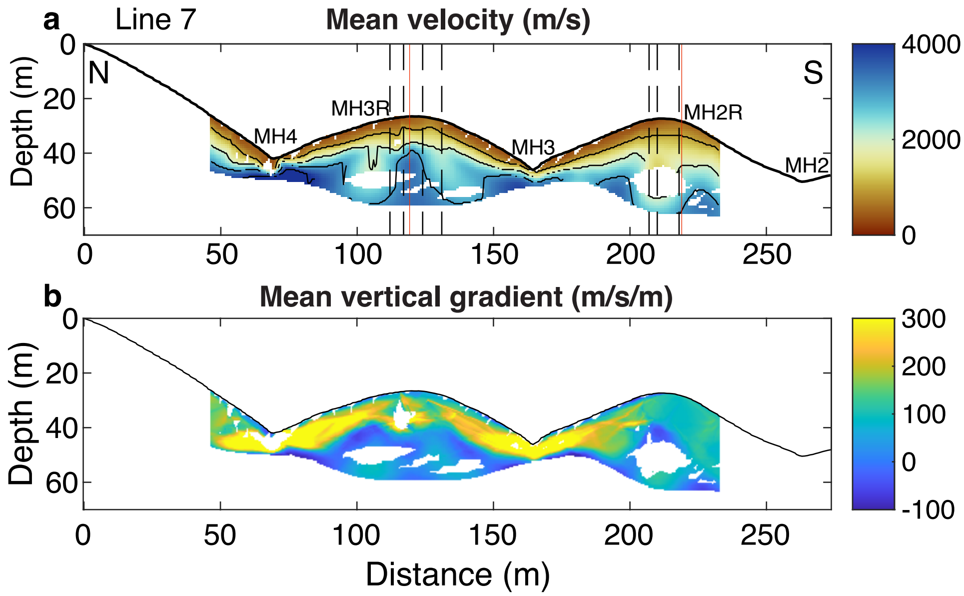

Figure 6. Results of Line 7 inversion. (**a**) Mean velocity model with contour lines at 1000, 2000, 3000, and 4000 m/s. The model is masked out below the deepest raypath and where CoV > 30%. Black dashed lines highlight the locations of boreholes within 10 m of the survey line. From north to south, these include boreholes MH3-W3, MH3-W4, MH3-W1, and MH3-W2 on MH3R, and MH3-W6, MH3-W5, and MH3-W7 on MH2R. The orange vertical lines indicate the intersection points of Line 7 with Lines 8 (MH3R) and Line 9 (MH2R). (**b**) Mean vertical gradient (m/s/m). Note the gradient color scale ranges from -100 to 300 m/s/m.

4.1.4 MH3R Perpendicular (Line 8)

Three boreholes at MH3R are within 10 m of Line 8: MH3-W1, MH3-W3, and MH3-W4. The velocity contours are surface-parallel for most of the west-facing slope, though the 3000 m/s contour is more variable (**Figure 7a**). The east-facing slope has a highly variable thickness of weathered material, with Vp > 2000 m/s reached at the surface near the ridgetop, and at > 25m depth towards the east channel. The shallow high-velocities east of the ridge correspond to the location of the east-dipping sandstone cap that tops each ridge. While the structure of east and west-facing slopes are different, there is not a consistent difference in weathered zone thickness (**Figure S12**). Bedding-perpendicular Line 9 also reveals subtle variations in velocity structure that may relate to lithologic contrasts (**Figure S5**), but the overall east and west-facing structures do not appear to differ dramatically. All bedding-perpendicular lines indicate largely surface-parallel weathered material that thins at the channel and thickens at the ridge.

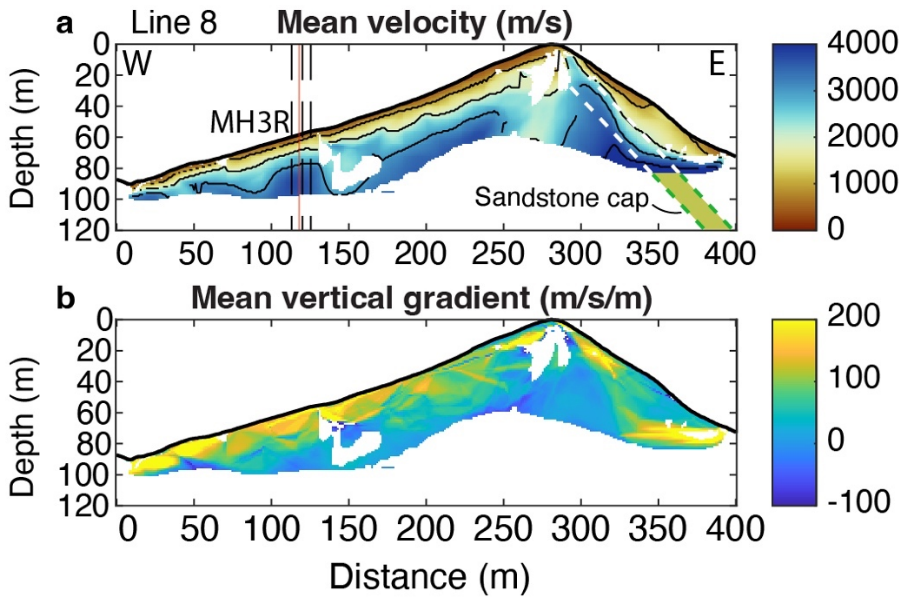

Figure 7. Results of Line 8 inversion using THB rj-MCMC. (**a**) Mean velocity model with contour lines at 1000, 2000, 3000, and 4000 m/s. The model is masked out below the deepest raypath and where CoV > 30%. Black dashed lines highlight the locations of boreholes within 10 m of the survey line. From west to east, this includes boreholes MH3-W4, MH3-W1, and MH3-W3. The orange vertical line indicates the intersection point with Line 7. The white and green dashed lines and SS represent the sandstone capstone. (**b**) Mean vertical gradient (m/s/m).

4.2 Borehole and Seismic Velocity Comparison

We do not attempt to analyze the soil layer (Interface 1, < 1 m; Pedrazas et al., 2021) using seismic velocity, as the seismic wavelength and p-wave picking uncertainty do not allow us to capture submeter structure. Using seismic refraction data, we can delineate deeper interfaces using a velocity contour, or with the peak velocity gradient. Here we present the results of both. Material above the Interface 2 depth (pervasively fractured saprolite) gradually increases in Vp from 400-1000 m/s. The average Vp across Interface 2 for all ridges is 1284 ± 203 m/s (**Figure 8**). For each ridge, the Interface 2 Vp varies with the orientation of the seismic line relative to bedrock bedding, with bedding-perpendicular lines often fastest. Uncertainty in the Interface 2 depth from borehole data also adds to the velocity range. Material below the Interface 2 depth (weathered bedrock) is generally 1300-2000 m/s. Average velocity corresponding to the Interface 3 depth is 1973 ± 435 m/s across all lines. Vp at Interface 3 differs significantly between the three ridges (**Figure 8**). Interpretation of Interface 3 from the borehole is based primarily on a decrease in yellowness hue with depth (inferred as a decrease of chemical weathering) and a decrease in fracture density (Pedrazas et al., 2021). However, the different Vp ranges for Interface 3 between ridges suggests these borehole changes may not map onto a specific velocity contour.

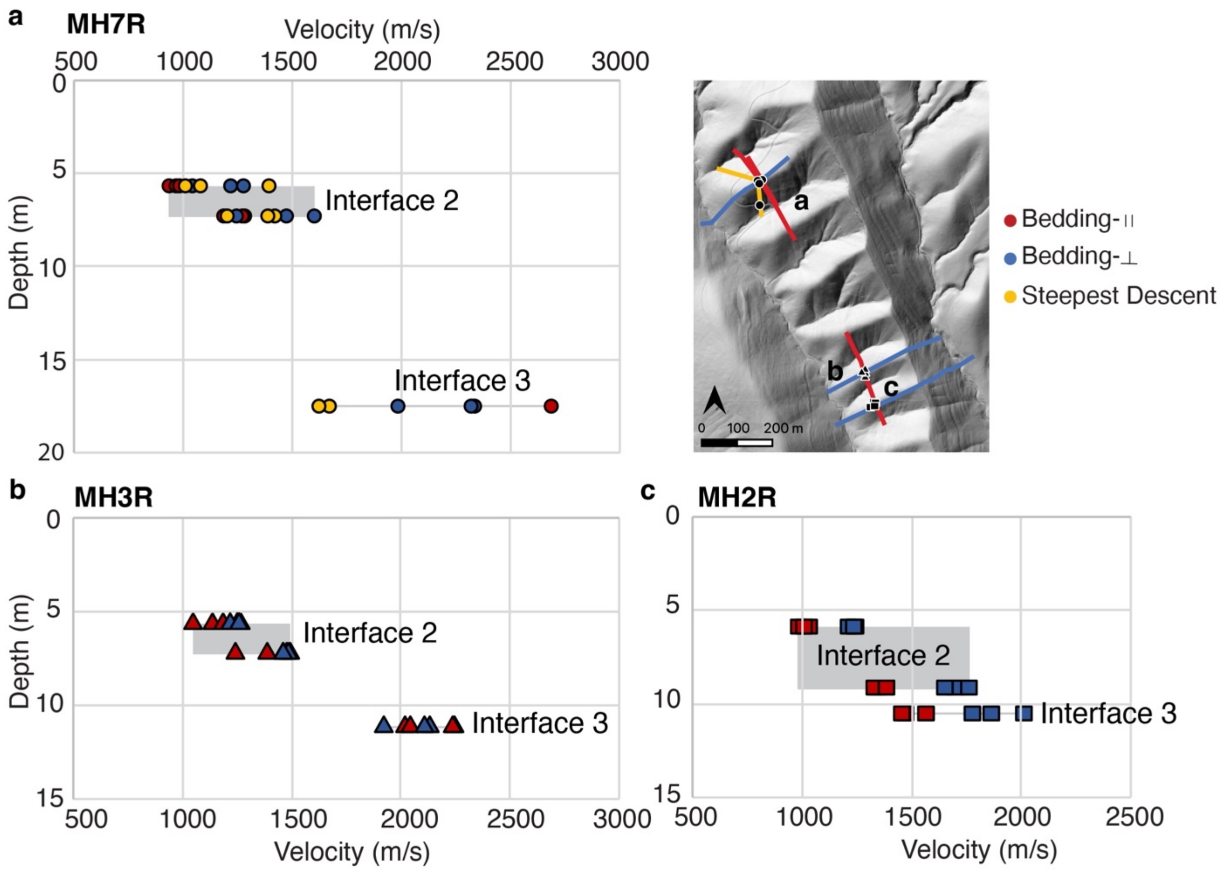

Figure 8. Seismic velocity at borehole interfaces 2 and 3 identified by Pedrazas et al. (2021) for (**a**) MH7R, (**b**) MH3R, and (**c**) MH2R. An upper and lower depth bound is plotted for Interface 2 based on the depth standard deviation from Pedrazas et al. (2021). Marker colors indicate the survey line orientation.

The maximum vertical velocity gradient captures the fastest increase of Vp with depth, likely due to rapid reduction of bulk porosity, which may be comparable to borehole interfaces. However, vertical velocity gradient does not exhibit a clear peak that can be easily traced across a hillslope. Rather, a zone of high gradient is observed in all profiles (**Figures 4c, 5b, and 7b**). At the MH7R ridgetop, we see a zone of high velocity gradient from around 3 m to 7–10 m depth (**Figure 9b**). At MH3R, this high gradient zone appears as 2 peaks centered at 3 m and 10 m. For MH2R, the high gradient zone is gradual without a clear peak, stretching from 2–12 m. There is not a clear relationship between velocity gradient and borehole property gradients (colored boxes in **Figure 9b**), but the most rapid changes in borehole properties do occur within the highest velocity gradient zone (~3–13 m) for each survey. Borehole transitions such as the increase in blowcount rate occur more gradually for MH2R (Pedrazas et al., 2021) consistent with its much lower velocity gradient.

Orientation of the seismic lines also has an effect on the gradient structure. Across all three ridges, bedding-parallel lines have more pronounced peak gradient features, and bedding-perpendicular lines show a more consistent gradient, reflective of a more gradual increase in velocity. It is difficult to distinguish Interfaces 2 and 3 using velocity gradient. Rather, a relatively high-gradient zone, across which borehole properties change most dramatically, spans both interfaces.

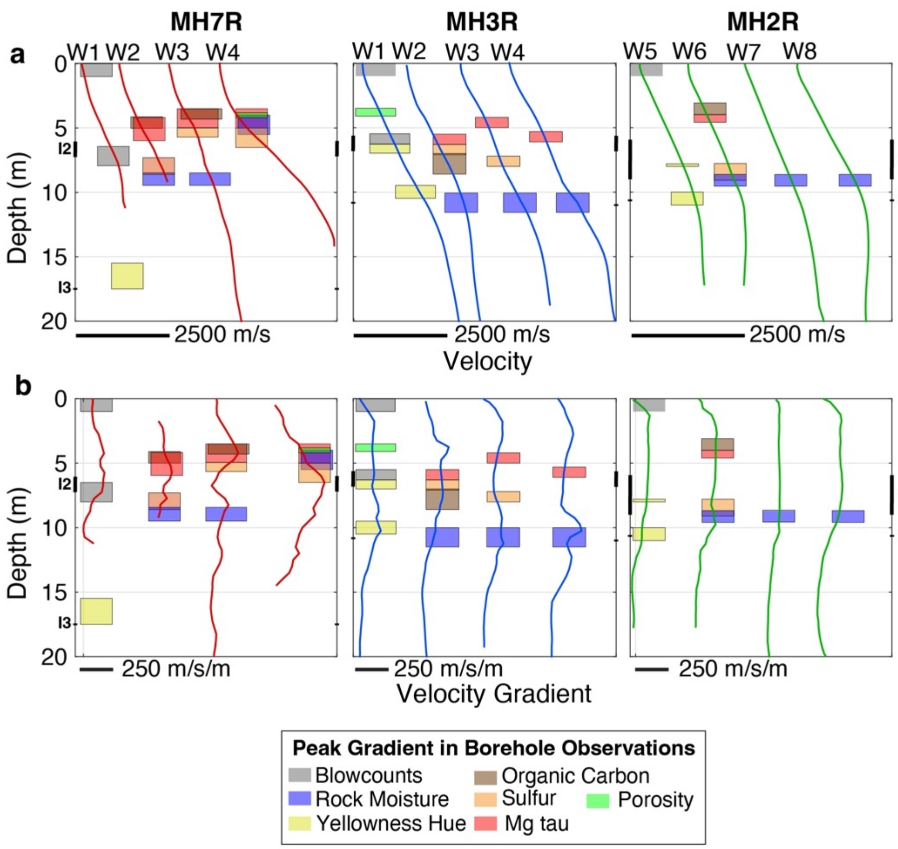

Figure 9. Velocity (a) and velocity gradient (b) profiles for each borehole across the three ridges. Each 1D profile represents the velocity and velocity gradient at each borehole averaged across all seismic line orientations. Colored boxes represent depth ranges where the vertical gradient of each borehole property is highest. Interface 2 (I2) and Interface 3 (I3) depths are shown on the edge of each plot (from Pedrazas et al., 2021). Only the deep boreholes MH7-W1, MH3-W1, and MH2-W5 have observations of blowcount rate and yellowness hue. The absence of a data type for a given profile indicates there were no sharp changes in that property with depth. The x-axis is stretched to space out each borehole, and a scale bar is shown for velocity and velocity gradient.

4.3 Hillslope Analysis

To examine aspect-dependency in the subsurface, we compare the depth to the saprolite-weathered bedrock transition (Interface 2, 1284 ± 203 m/s) and weathered-fractured bedrock transition (Interface 3, 1973 ± 435 m/s) on sets of north-facing and south-facing hillslopes that share the same ridge or the same catchment. **Figure 10** shows the depth to Interface 2 with distance from the ridge along a straight-line transect. For all hillslopes, the saprolite layer thickens towards the ridge, and the depth to the base of the saprolite appears nearly identical on north and south-facing slopes, though it is variable from channel to ridge (**Figure 10a**).

Averaged depths to the 700 m/s, 1284 m/s (Interface 2 contour), 1973 m/s (Interface 3 contour), 2500 m/s, and 3000 m/s velocity contours present an inconsistent relationship between aspect and velocity, with the average south-facing depth sometimes shallower and sometimes identical to north-facing slopes. When the Interface 2 depth is normalized with distance from the ridge, the MH7 south-facing slope appears to have a shallower Interface 2 depth than the MH7 or MH8 north-facing slopes. However, at MH2, the normalized south-facing slope has a greater Interface 2 depth. Normalized average depth to velocity contours similarly shows shallower weathering depth on the MH7 south-facing slope, but deeper or identical weathering depth on the MH2 south-facing slope. Interface 2 depths from boreholes do not provide enough constraint to identify a consistent pattern relating saprolite thickness to hillslope aspect. Through combined analysis with geophysics, we find no consistent difference in saprolite thickness with slope aspect for our surveyed ridges. This appears to be true for slopes within the same catchment (i.e., MH7 S and MH7 N), and for slopes sharing the same ridge (i.e., MH7 S and MH8 N).

We also compared Interface 2 depth between the MH8 north-facing and MH7 south-facing slopes along the steepest descent survey orientation (Lines 4 and 5; **Figure S7**. The steepest-descent profiles also do not demonstrate clear differences in Interface 3 depth between north-facing and south-facing slopes, although the Interface 3 depth does appear shallower below the MH7 south-facing slope in the mid-slope position (**Figure S9c,d**).

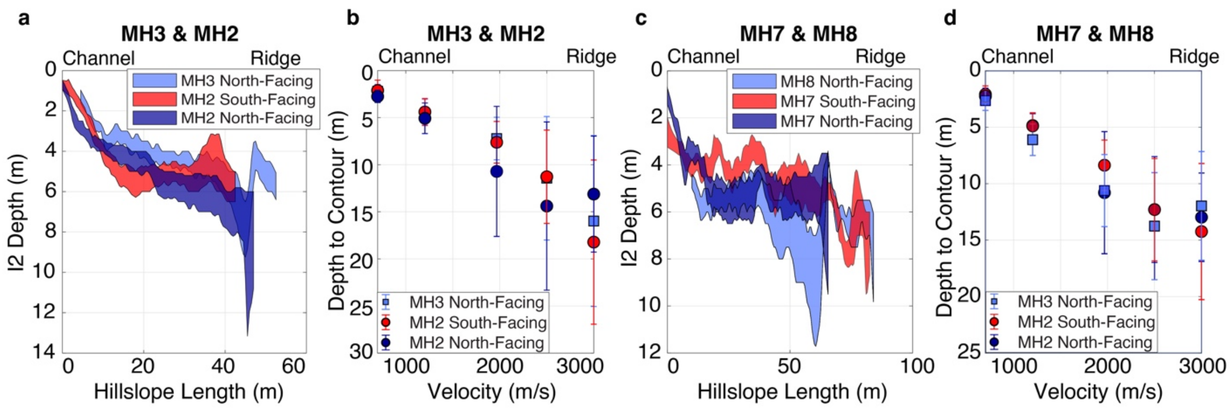

Figure 10. Comparison of weathering thickness on north- versus south-facing hillslopes for Line 6 (a-b), and Line 1 (c-d). Depth to Interface 2 (I2; saprolite-weathered bedrock) with hillslope length (**a,c**) is shown based on the I2 velocity range (1284 ± 203 m/s velocity contours). Average depths to various velocity contours are shown in (**b, d**), including the average Interface 2 velocity contour (1284 m/s) and average Interface 3 velocity contour (1973 m/s).

4.4 Trade-off between porosity and saturation

4.4.1 1D Porosity and Saturation at MH7

Following Section 3.3, our rock physics model result is a tradeoff between saturation and porosity that can equally describe the observed seismic velocity at depth. The relation between saturation and porosity is not linear. Below a certain threshold, changes in saturation do not affect the modeled porosity, while above this threshold, small increases in saturation necessitate dramatic increases in porosity to explain the same velocity observation (**Figure 11**). Though we lack direct saturation measurements at RV, volumetric water content estimated from repeat neutron probe counts indicates the volumetric water content is 25-35% for the first 10 m. As volumetric water content is the product of porosity and saturation (Equation 2), water content is equal to porosity when pores are fully saturated. This indicates that porosity must be at least 35% at the surface, and at least 30% at 6 m depth.

As shown in **Figure 11**, the porosity-saturation tradeoff estimated from water content (blue dashed line) intersects the porosity-saturation tradeoff estimated from velocity (red curve) at each depth to identify a value for porosity and saturation (black shade on curve). For MH7, porosity is ~ 55% at the surface, decreasing to ~42% by 5 m, and ~32% by 9 m. The modeled bulk porosities are much higher than the 12% maximum observed matrix porosity for MH7R (Pedrazas et al., 2021), consistent with significant inter-grain or fracture porosity. Porosity estimated from bulk τ is < 10% for the entire depth profile, so bulk τ alone is unable to explain the observed bulk or matrix porosities. Bulk τ is highest at a 3 m depth, indicating that porosity production from mass loss does contribute 30-50% of the matrix porosity within the saprolite layer.

Bulk porosity for MH3R and MH2R are shown in **Figures S10 and S11**, respectively. MH2R has higher bulk porosity in the upper 6m than MH3R or MH7R, consistent with the deeper low-velocity material observed in **Figure 6**.

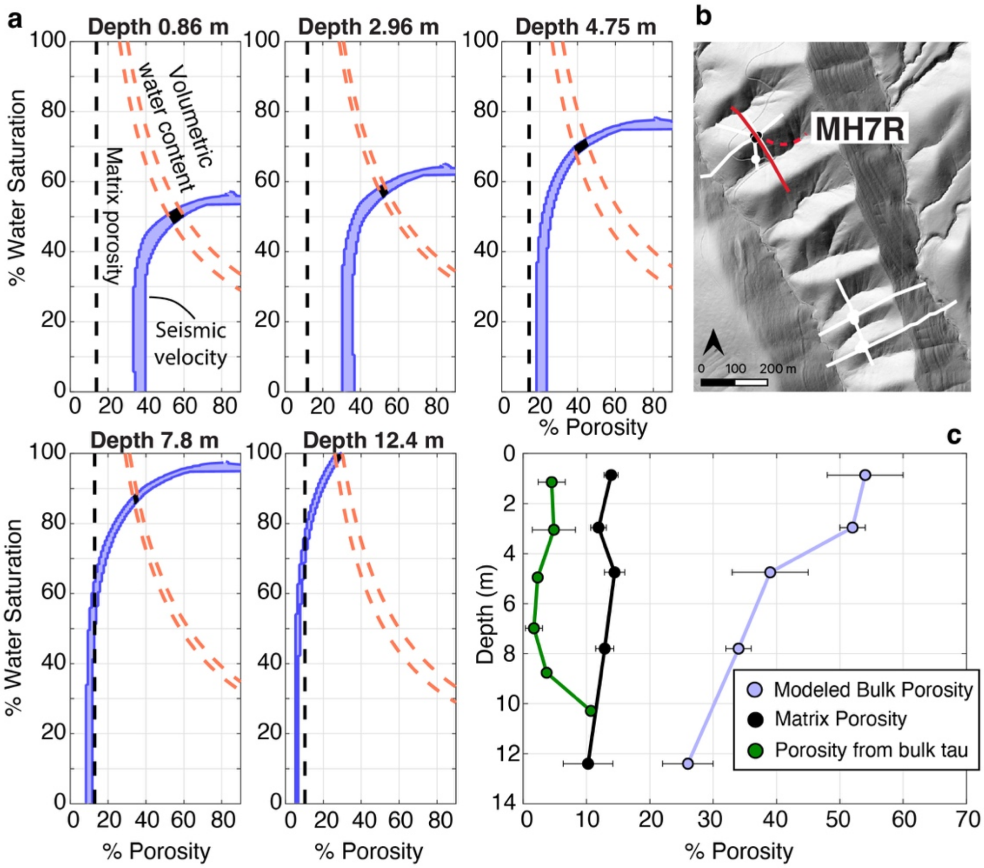

Figure 11. 1D rock physics model at MH7R (Line 1, a). (a) Tradeoff between saturation and porosity at MH7R at different depths. The thickness of the purple shaded area represents variation within a given mineral composition. The dashed black line is the measured matrix porosity from Pedrazas et al. (2021). The dashed red line indicates a tradeoff between porosity and saturation based on the volumetric water content measurement (Hahm et al., 2022). The black polygon indicates the inferred porosity and saturation based on both seismic refraction and the water content measurements. (**b**) Location of Line 1 (red line) and the boreholes used to measure volumetric water content (black circles). (**c**) Porosity with depth from the rock physics model (purple), the measured matrix porosity (black) and estimated from bulk τ (green), assuming no contribution to porosity from volumetric strain.

4.4.2 2D Porosity at MH7

The rock physics model can also be applied on a 2D scale to examine the landscape porosity distribution. 2D models show the most pronounced decrease in porosity occurs within the saprolite layer (< 6 m depth, **Figure 12**). Below this depth, porosity is low and only decreases gradually. The mean porosity models represent the average of porosity estimated using varied percentages of feldspar, quartz, and illite (see Section 3.3). Averaging porosity over a 20 m horizontal range at the ridgetop, our model indicates we can store up to 4.37 m of water in the top 15 m below the ridgetop, and 2.57 m in the top 6 m (**Figure S13**). The 2D model requires an assumed saturation distribution, which we based on neutron probe data corresponding to the month the seismic survey was taken (see Section 3.3). Assuming a different 2D saturation model would change the results of our model. When saturation is low, variation in the saturation model will not have a dramatic effect on porosity (**Figure 11a**). When water content is high, as is the case at RV from neutron probe estimates, small changes in saturation can cause a significant difference in the porosity value.

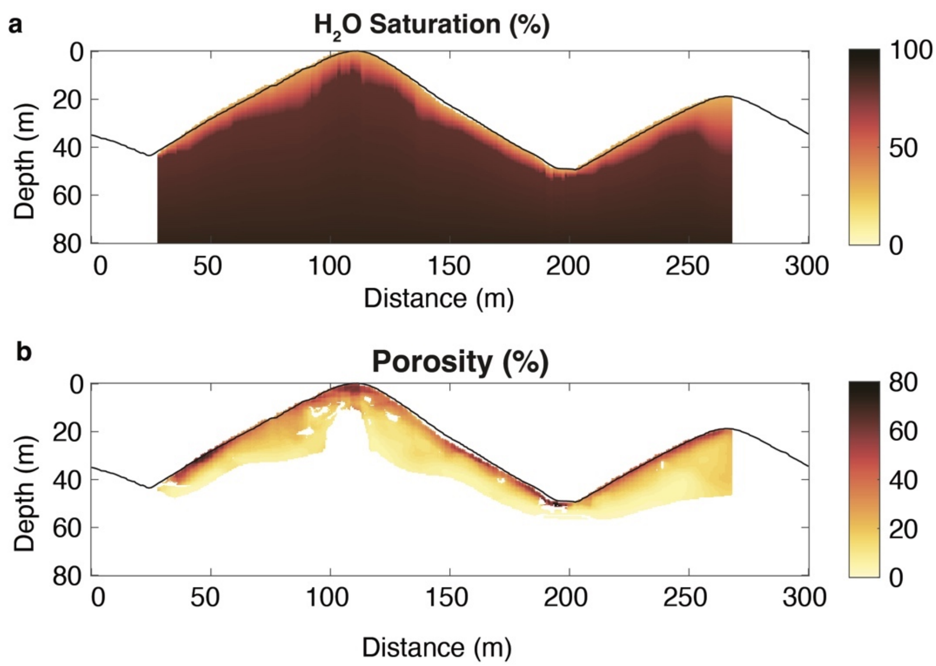

Figure 12. (**a**) A gradually increasing saturation model from 50-100% predicts (**b**) modeled bulk porosity averaged across different mineral compositions.

5. DISCUSSION

5.1 Borehole and Seismic Velocity Comparison

Seismic refraction is an ideal tool to determine broad scale subsurface structure by identifying transitions in velocity that can correspond to rock properties associated with weathering. However, seismic refraction is not expected to perfectly capture borehole-inferred properties since it is sensitive to larger spatial scales (meter-scale; Flinchum et al., 2022), whereas the borehole diameter is 6.35-12.7 cm and has cm-level sampling resolution for some measurements (Pedrazas et al., 2021). P-wave velocity (Vp) is a measurement of material strength, which depends on lithology, porosity, moisture content, and chemical weathering. Several studies have shown good agreement between Vp and rock strength or fracture density (e.g. Lee and de Freitas, 1990; Clarke and Burbank, 2011; Flinchum et al., 2018a; West et al., 2019; Holbrook et al., 2019), as well as chemical mass loss (Gu et al., 2020).

Seismic refraction surveys at RV capture a CZ structure that closely matches the borehole-derived structure presented by Pedrazas et al. (2021). Material with Vp < 1284 m/s is interpreted as saprolite, consistent with other studies that find saprolite Vp < 2000 m/s (Befus et al., 2011) or < 1200 m/s (Flinchum et al., 2018a; Leone et al., 2020). The core within this zone is "pervasively fractured," oxidized, and mechanically weak (Pedrazas et al., 2021). An increase in vertical velocity gradient occurs towards the bottom of the saprolite layer, marking a gradual transition to weathered bedrock. From the 1284 m/s contour, and the onset of the high gradient zone, we can determine the thickness of the saprolite across the landscape as 0 - 2 m thick at the channels, and increasing with lateral distance from the channel. Once it reaches 4-6 m depth, it remains this thick under most of the hillslope and increases only gradually near the ridgetop (**Figure 10a,c**). The depth to the saprolite is nearly identical between ridges, despite a 25 m difference in relief from MH7R to MH3R and MH2R.

Below the saprolite layer, Vp increases rapidly from ~1200 – 2000 m/s and then increases only gradually. This Vp range is variably thick across the landscape, and is inferred to be weathered bedrock based on the presence of open, oxidized fractures. The bottom of the weathered bedrock experiences a sudden drop in yellowness hue and decrease in fracture density from "discreetly" to "rarely" fractured (**Figures 2 & 9**; Pedrazas et al., 2021). The bottom of the weathered bedrock is also upslope-thickening (**Figure S9**). The transition from saprolite to weathered bedrock (Interface 2) and the transition from weathered to fractured bedrock (Interface 3) are difficult to distinguish using velocity contours or vertical velocity gradient, possibly because of differences in velocity measurements based on survey line orientation, and differences in lithology between ridges. The lack of a clear distinction between interfaces is also visible in the borehole data. For example, the depth of rock moisture storage from neutron probe counts at 8-9 m below ridgetops generally exceeds the Interface 2 depth (6 m) but not the Interface 3 depth (11-17 m). While we interpret a "layered" CZ structure, the layers we observe are part of a broad, gradual zone of physical and chemical weathering, starting a few meters below the surface, and extending to ~20 m below the ridgetops (**Figure 11**). This gradual zone of increasing material strength is similar to CZ models presented at Shale Hills (West et al., 2019) and Calhoun Observatory (Holbrook et al., 2019).

Velocity below the weathered bedrock is too low to correspond to fresh bedrock. Unweathered bedrock is more likely to be reached at ~20 m depth where velocities reach 3000 m/s and velocity gradient approaches zero. The material between the weathered and unweathered bedrock is interpreted as fractured bedrock, where Vp continues to increase from 2000 to > 3000 m/s, likely due to further reductions in fracture density with depth and an increase of overburden. The core at this depth is rarely fractured, and fractures present are closed and unoxidized (Pedrazas et al., 2021). When porosity is low, even a < 5 % decrease in crack volume can increase Vp by 1000 m/s in granites (Flinchum et al., 2022). Several studies use 4000 m/s as the bedrock velocity contour (Befus et al., 2011; Holbrook et al., 2014; Gu et al., 2020), however 3000 m/s is still within the expected range for unweathered sedimentary bedrock with 10% porosity (Eberhart-Phillips et al., 1989; Mavko 2009; Dvorkin et al., 2021). The core at the depth of the 3000 m/s contour is intact rock that is unweathered and rarely fractured (Pedrazas et al., 2021). Velocity below the channel surveys, which should be relatively fresh, are mostly <

4000 m/s (**Figures 5 & S6**). All of our surveys therefore reach fresh bedrock at or above the channel elevation, and we do not see a CZ topography that systematically mirrors surface topography as expected for a highly stressed tectonic environment (Moon et al., 2017).

From analysis of borehole data, seismic velocity, and vertical velocity gradient, we can characterize CZ structure at RV as including: (1) a thin (< 1 m) soil layer, (2) a ~ 5m thick saprolite layer that thins abruptly at the channels, across which porosity-producing chemical reactions occur and mechanical strength dramatically changes, (3) a weathered bedrock layer of high velocity gradient in which the presence of open, oxidized fractures gradually decrease, and (4) a variably thick fractured bedrock layer with closed, unoxidized fractures.

The sedimentary bedrock lithology has a distinct influence on the landscape at RV, with the main north-south ridge composed of a thick (> 10 m) sandstone cap and the valley east of the ridge mostly of shale (**Figure 1**). Line 8 features a high-velocity zone matching the location of the MH3R sandstone cap (**Figure 7**). We also observe a thicker CZ below MH2R than MH3R, likely because MH2R intersects a larger proportion of shale (Pedrazas et al., 2021; **Figure 6**). Bedding orientation plays a role in weathering processes and depth to bedrock weathering at RV. It may help to explain why different orientations of survey lines result in different Vp values (**Figure S3**). However, we do not find lithology to be a dominant control on CZ structure, as documented in metamorphic bedrocks (Leone et al., 2020). Based on the Vp results, the overall thickness of saprolite and weathered bedrock on bedding-parallel and bedding-perpendicular lines are similar, and we do not see a strong contrast between east and west-facing slopes despite the different intersection of bedding planes with surface topography (**Figure 7**).

5.2 Characterizing weathering across hillslopes

Seismic refraction method captures changes in the material properties of the subsurface, allowing us to project Interfaces 2 and 3 across the landscape. With these interfaces estimated at the landscape scale, we can explore how the landscape is organized and model properties of the subsurface.

5.2.1 North vs. South facing hillslopes

Several seismic refraction studies have observed thicker saprolite and weathered rock on north-facing slopes, and a thinner weathered layer on south-facing slopes (Befus et al., 2011; Nielsen et al., 2021; Olyphant et al., 2015; Wang et al., 2021). However, most of these sites have a different lithology and climate regime than RV, both of which are thought to affect the magnitude of asymmetry (Inbar et al., 2018; Pelletier et al., 2018) and the thickness of weathered material (Hahm et al., 2019).

Seismic refraction at RV does not show a clearly thicker saprolite layer on north-facing slopes (**Figure 10**), consistent with borehole observations from Pedrazas et al. (2021). This result is contrary to what we might expect in a precipitation-limited environment (as in Pelletier et al., 2018), where increased soil moisture and root-rock interactions on north-facing slopes can exert a top-down influence on CZ structure. The stark difference in vegetation (**Figure 1**) and the thicker soil profiles on north- versus south-facing hillslopes at RV indicate that aspect-dependent solar radiation does play a role in surface landscape processes (Pedrazas et al., 2021). Tree roots at RV can extend 14 m laterally and 6-8 m down into the weathered bedrock (Hahm et al., 2022), and are therefore likely to contribute to bedrock weathering through biochemical or biomechanical processes (Pawlik et al., 2016). However, the surveyed hillslopes do not provide clear evidence of aspect-dependent weathering below the soil layer at the spatial resolution of the seismic refraction data.

Other studies have also observed aspect-dependent vegetation density at sites without clear aspect-dependent saprolite thickness. For example, south-facing slopes of the Santa Catalina Mountains in Arizona have thicker saprolite, despite a lower tree density (Leone et al., 2020). This is attributed to the orientation of bedrock foliation planes, which dip into the surface topography at a high angle on the south-facing slope, and are oriented parallel to the north-facing slope. The high angle intersection on the south-facing slope facilitates enhanced weathering along the weak foliation planes, creating thicker saprolite. At RV, bedding and dominant fracture planes are oriented N10°E, therefore the apparent dip of the lithology and the most abundant fracture set is nearly horizontal for the bedding-parallel seismic survey lines, implying no significant difference in the angle between bedding or fracture planes and surface topography for north versus south-facing slopes. Therefore, increased hydraulic conductivity along planes of weakness does not explain the lack of north/south aspect-dependency below the soil layer at RV. There is a strong contrast in the angle of bedding and fracture planes relative to the surface on east versus west-facing slopes, but the bedding-perpendicular lines also do not indicate a substantial difference in saprolite thickness on east versus west-facing slopes (**Figure S12**).

A plausible explanation for north and south-facing slopes having the same saprolite depth is that weathering processes at RV have not always been precipitation-limited. During the Pleistocene, RV experienced a cooler, wetter climate that may have resulted in minimal differences in tree density with aspect (Cole, 1983; Adams and West, 1983). As the climate has shifted to drier and warmer conditions in the last few thousand years, the tree population may have adjusted. However, the time scale required for weathering bedrock is typically much longer than glacial cycles (tens of thousands of years), which may explain the lack of deeper aspect differences. The influence of past climate on aspect differences has been documented across many regions. At Shale Hills in Pennsylvania, frost-cracking during the last glacial maximum interacted with microtopography to drive the hillslope asymmetry observed today, despite a lack of frost-cracking conditions in the present climate (West et al., 2019; Wang et al., 2021). Likewise, the strong slope asymmetry currently observed in the Redondo Mountains in New Mexico can be explained by vegetation regimes present in the cooler Pleistocene (Istanbulluoglu, 2008).

5.2.2 Porosity

Several recent studies have applied rock physics models to estimate porosity from seismic refraction data (e.g. Holbrook et al., 2014; Flinchum et al., 2018a,b; Hayes et al., 2019; Gu et al., 2020; Callahan et al., 2020). The parameters known to influence Vp include elastic moduli of the mineral composition, porosity of the material, and saturation level. Without direct measurements of saturation, the rock physics model at RV explores a nonlinear relationship between porosity and saturation (**Figure 11**). Using volumetric water content estimates from down-hole neutron counts, we can roughly constrain porosity with depth. Estimating water content from neutron counts has an uncertainty of 5% and may be less accurate at greater depths (Hahm et al., 2022). The high volumetric water content with depth at RV, combined with the seismic velocity data, estimate a saturation of 100% by a 12 m depth (**Figure 11a**). However, we do not reach a water table within 12 m (Hahm et al., 2022; Pedrazas et al., 2021), therefore saturation is likely less than 100%. Our porosity estimates may therefore represent an upper limit on porosity.

Furthermore, we only have neutron counts at borehole locations, and saturation at the hillslope scale is likely more heterogeneous than any assumed laterally homogeneous saturation model. Our porosity modeling results nonetheless indicate that even at sites without extensive saturation measurements, the tradeoff between porosity and saturation provides valuable insight into water storage dynamics, which can be further constrained by seismic surveys collected in different seasons, or downhole data such as neutron counts.

Our results provide a porosity distribution ranging from 60% at the surface to ~30% at a 9 m depth, higher than the measured matrix porosities from Pedrazas et al. (2021). This discrepancy is expected given that matrix porosities were based on chips removed from the core, which can be biased when the core matrix material is pervasively fractured. Measured matrix porosity below 10-15 m is likely to be more representative of the bulk porosity since this depth of material is less fractured. Matrix porosity is < 10% below 20 m, indicating a 20% decrease in porosity from the base of the saprolite to the rarely fractured bedrock (Pedrazas et al., 2021). Like results from the Sierra Nevada Critical Zone Observatory (Hayes et al., 2019), bulk τ cannot be the sole factor in porosity production at RV (**Figure 11c**). Porosity predicted from mass loss suggests that chemical depletion generates a high fraction of the total modeled porosity in the saprolite but contributes little to no porosity production elsewhere in the depth profile. The higher porosities modeled from Vp therefore reflect the presence of fractures, possibly due to mass unloading, in addition to chemical depletion.

As in Callahan et al. (2020), mineralogy does not have a large influence on porosity. Despite sharing a similar sedimentary lithology, porosity at Shale Hills is systematically lower than RV, with a maximum porosity of only 30% (Gu et al., 2020). RV's shallow porosity distribution is more like that of the granitic Sierra Nevada Mountains, which ranges from 50-70% at the surface, to 20-30% at the base of the saprolite (Hayes et al., 2019; Callahan et al., 2020). RV and the Sierra Nevada sites may share a more similar porosity distribution due to fractures driven by regional tectonic activity.

Seismic refraction surveys greatly improve our ability to analyze water storage at RV by allowing us to estimate water-holding capacity from bulk porosity. Measurements from cores do not always accurately represent bulk porosity due to limited spatial sampling (Callahan et al., 2020). Water-holding capacity is distinct from the dynamic root zone storage (~300 mm, Hahm et al., 2022), which can inform plant vulnerability to prolonged drought on annual timescales. Our estimate instead provides a measure of the total water that could be stored in the hill. Water-holding capacity may be indicative of longer-term climate shifts, with wetter climates facilitating deeper weathering and larger storage capacity (e.g. Anderson et al., 2019). The water-holding capacity at RV is at least 8 times greater than the average annual rainfall of 534 mm/yr, suggesting the thick CZ structure may be largely a product of the wetter Pleistocene climate regime. While water-holding capacity may not directly tell us about ecosystem response to future climate shifts, understanding the water storage potential of a landscape is crucial to understanding hydrologic dynamics overtime (East and Sankey, 2020).

5.3 Broader implications to Critical Zone Models

Weathering structure at RV can inform mechanistic features of critical zone development in semi-arid landscapes. Upslope thickening topography of the weathered layers suggests that the hydraulic conductivity model proposed by Rempe and Dietrich (2014), in which drainage of chemically equilibrated groundwater controls the fresh bedrock boundary, could apply to this landscape. This model predicts a permanent water table limiting the extent of chemical weathering reactions, but we find no evidence of a permanent water table at RV within the depth range of the weathered zone (Hahm et al., 2022; Pedrazas et al., 2021). Water was observed in the boreholes 30-35 m below the surface for MH7R, and 15-21m below the surface for MH3R and MH2R (Hahm et al., 2022; Pedrazas et al., 2021). However, the current water table at RV may not necessarily align with the interface depths since the water table may have dropped since the cooler and wetter climate of the Pleistocene. Alternatively, the nested reaction fronts proposed by Lebedeva and Brantley (2013) and Brantley et al. (2017) could describe RV's weathering structure. Lebedeva and Brantley (2020) show that in settings with low infiltration rate, reaction fronts can be located above the water table.

With regard of the weathering structure of the ridge-valley system at RV, Pedrazas et al. (2021) found a roughly linear scaling relationship between hillslope length and relief of interfaces 2 and 3, which agrees with the predicted depth to fresh bedrock (Zb) location by Rempe and Dietrich (2014). In this study, we expand this analysis to 2D using the seismic velocity models. There are 6 channel-to-ridgetop transects that can be drawn from 2 seismic lines (lines 1 & 7). We plot the 6 seismic refraction-based interface 3 topography (**Figure S14a**) and find that the scaling relationship of interface 3 elevation below the ridgetops appears to be non-linear, as shown by the black dash line in **Figure S14a**. Additionally, if the CZ structure scales linearly, the normalized 2D geometry of interface 3 should be identical. However, the geometry of the interface 3 does not appear to be identical after we normalize the hillslope length (**Figure S14b**). This result contradicts the finding by Pedrazas et al. (2021), which solely using borehole data. Our results suggest that there could be more localization of channel incision rate and/or bedrock hydraulic conductivity that varies between different catchments.

The ratio of gravitational and horizontal tectonic stresses can also determine the potential of subsurface fracturing and create deep weathering extending below the elevation of the channel in high-compressional regimes (St. Clair et al., 2015; Moon et al., 2017). At RV, the lack of surface-mirroring weathering implies lower tectonic stress parallel to the bedding strike (St. Clair et al., 2015). However, RV is less than 30 km away from the Bartlett Springs Fault system, and the principal compressive stress has been oriented roughly N-S (parallel to the bedding strike) for at least the past 5 Ma (Atwater and Stock, 1998). With a contemporary maximum shear strain rate of ~50-100 nano-strain/yr (Zeng et al., 2018; Xu et al., 2020), we consider RV subject to a relatively high tectonic stressing rate. Even though the current tectonic stressing rate is high, high internal strain rate and micro-fractures generated by ground motion from regional earthquake events may decrease material strength at RV. This adds additional complexity to estimating fracture distribution from a simple stress model. In contrast, although current tectonic strain rate is low on the east coast of the US (< 2 nano-strain/yr; Kreemer et al., 2018), hydraulic fracturing tests indicate a higher tectonic stress (generally greater than a few MPa; Heidbach et al., 2016) that can be associated with higher material strength. This may explain a mirror image of surface topography in CZ structure at multiple sites on the east coast, as suggested by St. Clair et al. (2015). This finding may suggest that stress measurements from borehole breakout and hydraulic fracturing tests may be a more relevant method for estimating absolute stress and material strength in shallow crust.

6. CONCLUSIONS

Through a combination of near-surface geophysics and direct observations from boreholes, we are able to characterize critical zone structure at Rancho Venada, a semi-arid, sedimentary ridge-valley landscape in northern California. Seismic data alone reveals a weathered zone from 4-13 m below ridgetops, over which velocity increases from ~1000 – 2500 m/s. In combination with borehole data, we can detect a transition from pervasively fractured and chemically weathered material, to more competent material at a 5-6 m depth, corresponding to a velocity range of 1284 ± 203 m/s. This transition is interpreted as the saprolite-weathered bedrock transition, and is largely surface-parallel, with a slight thickening towards the ridges and sharp thinning at the channels. A second, deeper transition zone is observed in the borehole logs, as yellowness hue further decreases, corresponding to a velocity range of 1973 ± 435 m/s. We interpret the deeper transition as the weathered - fractured bedrock boundary. Bedding-parallel and bedding-perpendicular lines indicate the weathered zone thins towards the main channel in the west, and towards the subchannels to the north and south.

Despite higher tree density and thicker soils on north-facing slopes, we observe an overall similar saprolite and weathered bedrock layer on both north- and south-facing slopes, contrary to what we might expect in a precipitation-limited environment. The cooler, wetter climate RV experienced during the Pleistocene may have allowed for the presence of trees on both hillslopes, creating equally thick saprolite layers that have not yet adjusted to the current climate condition. Porosity production at RV is similar to igneous sites in the Sierra Nevada and is likely dominated by fractures rather than chemical weathering.

7. Acknowledgements

We thank the Brown and the Hemmi families for providing site access. We are grateful for field assistance from Anna Weniger, Colleen Murphy, Jeng-Hann Chong, Kristen Fauria, and Maryn Sanders to carry out the seismic refraction surveys. We also like to think Bill Dietrich, Kristen Fauria, and Alex Bryk for their insights and significant contributions in the earlier phase of the research. BHR is supported by the Carleton College Paglia post-baccalaureate fellowship. Part of this research is contributed by NSF-EAR-2012616.

8. Data Availability Statement

Borehole data sets are published in Pedrazas et al. (2021). Volumetric water content and water table depths are published in Hahm et al. (2022). The THB rj-MCMC inversion is available on Zenodo (http://doi.org/10.5281/zenodo.4590999) and actively maintained in Github (https://github.com/MongHanHuang/THB_rjMCMC).

9. References

Adam, D. P., & West, G. J. (1983). Temperature and Precipitation Estimates Through the Last Glacial Cycle from Clear Lake, California, Pollen Data. *Science*, 219, 168-170.

Anderson, R. S., Anderson, S. P., & Tucker, G. E. (2013). Rock damage and regolith transport by frost: An example of climate modulation of the geomorphology of the critical zone. *Earth Surface Processes and Landforms*, 38(3), 299–316. https://doi.org/10.1002/esp.3330

Anderson, S. P., Hinckley, E-L., Kelly, P., & Langston, A. (2014). Variation in critical zone processes and architecture across slope aspects. *Procedia Earth and Planetary Science*, 10, 28-33.

Anderson, R. S., Rajaram, H., & Anderson, S. P. (2019). Climate driven coevolution of weathering profiles and hillslope topography generates dramatic differences in critical zone architecture. *Hydrological Processes*, 33(1), 4–19.

Atwater, T., & Stock, J. (1998). Pacific-north america plate tectonics of the neogene southwestern united states: an update. *International Geology Review*, 40(5), 375–402.

Bale, C. L., Williams, J. B., & Charley, J. L. (1998). The impact of aspect on forest structure and floristics in some Eastern Australian sites. *Forest and Ecology Management*, 110, 363-377.

Befus, K. M., Sheehan, A. F., Leopold, M., Anderson, S. P., & Anderson, R. S. (2011). Seismic constraints on critical zone architecture, Boulder Creek Watershed, Front Range, Colorado. *Vadose Zone*, 10, 915-927.

Brantley, S. L., Holleran, M. E., Jin, L., & Bazilevskaya, E. (2013). Probing deep weathering in the Shale Hills Critical Zone Observatory, Pennsylvania (USA): The hypothesis of nested chemical reaction fronts in the subsurface. *Earth Surface Processes and Landforms*, 38(11), 1280–1298. https://doi.org/10.1002/esp.3415

Brantley, S. L., Lebedeva, M. I., Balashov, V. N., Singha, K., Sullivan, P. L., & Stinchcomb, G. (2017). Toward a conceptual model relating chemical reaction fronts to water flow paths in hills. *Geomorphology*, 277, 100-117.

Brooks, P. D., Chorover, J., Fan, Y., Godsey, S. E., Maxwell, R. M., McNamara, J. P., & Tague, C. (2015). Hydrological partitioning in the critical zone: Recent advances and opportunities for developing transferable understanding of water cycle dynamics. *Water Resources Research,* 51, 6973–6987. doi:10.1002/2015WR017039.

Burdick, S., & Lekic, V. (2017). Velocity variations and uncertainty from transdimensional P-wave tomography of North America. *Geophys. J. Int.*, 209, 1337-1351.

Buss, H. L., Brantley, S. L., Scatena, F. N., Bazilievskaya, E. A., Blum, A., Schulz, M., Jiménez, R., et al. (2013). Probing the deep critical zone beneath the Luquillo Experimental Forest, Puerto Rico. *Earth Surface Processes and Landforms*, 38(10), 1170–1186. https://doi.org/10.1002/esp.3409

Buss, H. L., Lara, M. C., Moore, O. W., Kurtz, A. C., Schulz, M. S., & White, A. F. (2017). Lithological influences on contemporary and long-term regolith weathering at the Luqillo Critical Zone Observatory. *Geochimica et Cosmochimica Acta*, 196, 224-251.

Callahan, R. P., Riebe, C. S., Pasquet, S., Ferrier, K. L., Grana, D., Sklar, L. S., Taylor, N. J., et al. (2020). Subsurface weathering revealed in hillslope-integrated porosity distributions. *Geophysical Research Letters*, 47. https://doi.org/10/1029/2020GL088322.

Clarke, B. A., & Burbank, D. W. (2011). Quantifying bedrock-fracture patterns within the shallow subsurface: Implications for rock mass strength, bedrock landslides, and erodibility. *Journal of Geophysical Research*, 116. doi:10.1029/2011JF001987

Cole, K. (1983). Late Pleistocene Vegetation of Kings Canyon, Sierra Nevada, California. *Quaternary Research*, 19, 117-129.

Dawson, T. E., Hahm, W. J., & Crutchfield-Peters, K. (2020). Digging deeper: What the critical zone perspective adds to the study of plant ecophysiology. *New Phytologist*, 226, 666–671. https://doi.org/10.1111/nph.16410

Dietrich, W. (2019). High resolution mapping of antelope valley ranch, ca. National Center for Airborne Laser Mapping (NCALM). https://doi.org/10.5069/G9QC01MQ

Dvorkin J, Walls, J., & Davalos, G. (2021). Velocity-Porosity-Mineralogy Model for Unconventional Shale and Its Applications to Digital Rock Physics. *Front. Earth Sci.*, 8. doi:10.3389/feart.2020.613716

East, A. E., & Sankey, J. B. (2020). Geomorphic and sedimentary effects of modern climate change: Current and anticipated future conditions in the western United States. Reviews of Geophysics, 58. https://doi.org/10.1029/2019RG000692

Eberhart-Phillips, D., Han, D.-H., & Zoback, M. D. (1989). Empirical relationships among seismic velocity, effective pressure, porosity, and clay content in sandstone. *Geophysics*, 54(1), 82-89.

Flinchum, B. A., Holbrook, W. S., Rempe, D., Moon, S., Riebe, C. S., Carr, B. J., Hayes, J. L., St Clair, J., and Peters, M. P. (2018). Critical zone structure under a granite ridge inferred from drilling and three-dimensional seismic refraction data. *Journal of Geophysical Research*, 123: 1317–1343.

Flinchum, B. A., Holbrook, W. S., Grana, D., Parsekian, A. D., Carr, B. J., Hayes, J. L., & Jiao, J. (2018). Estimating the water holding capacity of the critical zone using near-surface geophysics. *Hydrological Processes*, 32, 3308-3326.

Flinchum, B. A., Holbrook, W. S., & Carr, B. J. (2022). What Do P-Wave Velocities Tell Us About the Critical Zone? *Front. Water*, 3. https://doi.org/10.3389/frwa.2021.772185

Godderis, Y., & Brantley, S. L. (2013). Earthcasting the future critical zone. *Elementa*, 1. doi: 10.12952/journal.elementa.000019

Grana, D., Parsekian, A. D., Flinchum, B. A., Callahan, R. P., Smeltz, N. Y., Li, A., Hayes, J. L., et al. (2022). Geostatistical Rock Physics Inversion for Predicting the Spatial Distribution of Porosity and Saturation in the Critical Zone. *Math Geosci*. https://doi.org/10.1007/s11004-022-10006-0

Gu, X., Mavko, G., Ma, L., Oakley, D., Accardo, N., Carr, B. J., Nyblade, A. A., et al. (2020). Seismic refraction tracks porosity generation and possible CO2 production at depth under a headwater catchment. *PNAS*.

Hahm, W. J., Riebe, C. S., Lukens, C. E., & Araki, S. (2014). Bedrock composition regulates mountain ecosystems and landscape evolution. *PNAS*, 111, 3338-3343.

Hahm, W. J., Dralle, D. N., Rempe, D. M., Bryk, A. B., Thompson, S. E., Dawson, T. E., & Dietrich, W. E. (2019). Low subsurface water storage capacity relative to annual rainfall decouples mediterranean plant productivity and water use from rainfall variability. *Geophysical Research Letters*, 46, 6544–6553. https://doi.org/10.1029/2019gl083294

Hahm, W. J., Rempe, D. M., Dralle, D. N., Dawson, T. E., Lovill, S. M., Bryk, A. B., & Dietrich, W. E. (2019). Lithologically controlled subsurface critical zone thickness and water storage capacity determine regional plant community composition. *Water Resources Research*, 55(4), 3028–3055. https://doi.org/10.1029/2018WR023760

Hahm, W. J., Dralle, D. N., Sanders, M., Bryk, A. B., Fauria, K. E., Huang, M. H., Hudson-Rasmussen, B., et al. (2022). Bedrock vadose zone storage dynamics under extreme drought: Consequences for plant water availability, recharge, and runoff. *Water Resources Research*, 58. https://doi.org/10.1029/2021WR031781

Handwerger, A. L., Huang, M-H., Fielding, E. J., Booth, A. M., & Burgmann, R. (2019). A shift from drought to extreme rainfall drives a stable landslide to catastrophic failure. *Scientific Reports*, 9. https://doi.org/10.1038/s41598-018-38300-0

Hayes, J. L., Riebe, C. S., Holbrook, W. S., Flinchum, B. A., & Hartsough, P. C. (2019). Porosity production in weathered rock: Where volumetric strain dominates over chemical mass loss. *Science Advances*, 5. https://doi.org/10.1126/sciadv.aao0834.

Heidbach, O., Rajabi, M., Cui, X., Fuchs, K., Müller, B., Reinecker, J., Reiter, K., et al. (2018). The World Stress Map database release 2016: Crustal stress pattern across scales. *Tectonophysics*, 744, 484-498. http://doi.org/10.1016/j.tecto.2018.07.007

Helgerud, M. B., Dvorkin, J., Nur, A., Sakai, A., & Collett, T. (1999). Elastic-wave velocity in marine sediments with gas hydrates: Effective medium modeling. *Geophysical Research Letters*, 26, 2021-2024.

Holbrook, W. S., Riebe, C. S., Elwaseif, M., Hayes, J. L., Harry, D. L., Basler-Reeder, K., Malazian, A. (2014). Geophysical constraints on deep weathering and water storage potential in the Southern Sierra Critical Zone Observatory. *Earth Surface Processes Landforms*, 39, 366–380.

Holbrook, W. S., Marcon, V., Bacon, A. R., Brantley, S. L., Carr, B. J., Flinchum, B. A., & Riebe, C. S. (2019). Links between physical and chemical weathering inferred from a 65-m-deep borehole through Earth's critical zone. *Scientific Reports*, 9(1), 4495. https://doi.org/10.1038/s41598-019-40819-9

Huang, M.-H., Hudson-Rasmussen, B., Burdick, S., Lekic, V., Nelson, M. D., Fauria, K. E., & Schmerr, N. (2021). Bayesian seismic refraction inversion for critical zone science and near-surface applications. *Geochemistry, Geophysics, Geosystems*, 22(5). https://doi.org/10.1029/2020GC009172

Inbar, A., Nyman, P., Rengers, F. K., Lane, P. N. J., & Sheridan, G. J. (2018). Climate dictates magnitude of asymmetry in soil depth and hillslope gradient. *Geophysical Research Letters*, 45, 6514–6522.

Istanbulluoglu, E., Yetemen, O., Vivoni, E. R., Gutiérrez-Jurado, H. A., & Bras, R. L. (2008). Eco-geomorphic implications of hillslope aspect: Inferences from analysis of landscape morphology in central New Mexico. *Geophysical Research Letters*, 35.

Klos, P. Z., Goulden, M. L., Riebe, C. S., Tague, C. L., O'Geen, A. T., Flinchum, B. A., Safeeq, M., et al. (2018). Subsurface plant-accessible water in mountain ecosystems with a Mediterranean climate. *WIREs Water*, 5. https://doi.org/10.1002/wat2.1277

Kreemer, C., Hammond, W. C., & Blewitt, G. (2018). A robust estimation of the 3-D intraplate deformation of the North American plate from GPS. *Journal of Geophysical Research: Solid Earth*, 123, 4388– 4412. https://doi.org/10.1029/2017JB015257

Lebedeva, M. I., & Brantley, S. L. (2013). Exploring geochemical controls on weathering and erosion of convex hillslopes: beyond the empirical regolith production function. *ESPL*, 38, 1793-1807.

Lebedeva, M. I., and Brantley, S. L. (2020). Relating the depth of the water table to the depth of weathering. *Earth Surf. Process. Landforms*, 45: 2167– 2178. https://doi.org/10.1002/esp.4873

Lee, S. G., & de Freitas, M. H. (1990). Seismic refraction surveys for predicting the intensity and depth of weathering and fracturing in granitic masses. *Field Testing in Engineering*, 6.

Leone, J. D., Holbrook, W. S., Riebe, C. S., Chorover, J., Ferré, T. P. A., Carr, B. J., & Callahan, R. P. (2020). Strong slope-aspect control of regolith thickness by bedrock foliation. *Earth Surface Processes and Landforms*, 45, 2998–3010. https://doi.org/10.1002/esp.4947

Mavko, M., Mukerji, T., & Dvorkin, J. (2009). Appendices. *The rock physics handbook: Tools for seismic analysis of porous media* (pp. 437–478). Cambridge: Cambridge University Press.

McCormick, E. L., Dralle, D. N., Hahm, W. J., Tune, A. K., Schmidt, L. M., Chadwick, K. D., & Rempe, D. M. (2021). Widespread woody plant use of water stored in bedrock. Nature, 597 (7875), 225–229. https://doi.org/10.1038/s41586-021-03761-3

Metropolis, N., Rosenbluth, A. W., Rosenbluth, M. N., Teller, A. H., & Teller, E. (1953). Equation of state calculations by fast computing machines. *The Journal of Chemical Physics*, 21, 1087–1092. https://doi.org/10.1063/1.1699114

Moon, S., Perron, J. T., Martel, S. J., Holbrook, W. S., & St Clair, J. (2017). A model of three-dimensional topographic stresses with implications for bedrock fractures, surface processes, and landscape evolution. *Journal of Geophysical Research: Earth Surface*, 122(4), 823–846. https://doi.org/10.1002/2016JF004155

Moon, S., Perron, J. T., Martel, S. J., Goodfellow, B. W., Ivars, D. M., Hall, A., Heyman, J., et al. (2020). Present-day stress field influences bedrock fracture openness deep into the subsurface. *Geophysical Research Letters*, 47. https://doi.org/10.1029/e2020GL090581

Nelson, M. D., Bryk, A. B., Fauria, K., Huang, M. H., & Dietrich, W. E. (2017). Physical properties of shallow landslides and their role in landscape evolution investigated with ultrahigh-resolution lidar data and aerial imagery. AGU fall meeting Abstracts.

Nielsen, T., Bradford, J., Holbrook, W. S., & Seyfried, M. (2021). The effect of aspect and elevation on critical zone architecture in the Reynolds Creek Critical Zone Observatory: A seismic refraction study. *Frontiers in Water*, 3, 670524.

Orlando, J., Comas, X., Hynek, S. A., Buss, H. L., & Brantley, S. L. (2016). Architecture of the deep critical zone in the Rio Icacos watershed (Luqillo Critical Zone Observatory, Puerto Rico) inferred from drilling and ground penetrating radar (GPR). *Earth Surface Processes*, 41, 1826-1840.

Parsekian, A. D., Singha, K., Minsley, B. J., Holbrook, W. S., & Slater, L. (2015). Multiscale geophysical imaging of the critical zone, *Rev. Geophys.*, 53, 1–26. doi:10.1002/2014RG000465.

Pawlik, L., Phillips, J. D., & Samonil, P. (2016). Roots, rock, and regolith: Biomechanical and biochemical weathering by trees and its impact on hillslopes—A critical literature review. *Earth-Science Reviews,* 159, 142–159. https://doi.org/10.1016/j.earscirev.2016.06.002

Pedrazas, M. A., Hahm, W. J., Huang, M.-H., Dralle, D., Nelson, M. D., Breunig, R. E., Fauria, K. E., et al. (2021). The relationship between topography, bedrock weathering, and water storage across a sequence of ridges and valleys. *Journal of Geophysical Research: Earth Surface*, 126(4). https://doi.org/10.1029/2020JF005848

Pelletier, J. D., Barron-Gafford, G. A., Gutiérrez-Jurado, H., Hinckley, E. S., Istanbulluoglu, E., McGuire, L. A., Niu., G.-Y., et al. (2018). Which way do you lean? Using slope aspect variations to understand critical zone processes and feedbacks. *Earth Surface Processes and Landforms* 43: 1133–1154.

Rempe, D. M., & Dietrich, W. E. (2014). A bottom-up control on fresh-bedrock topography under landscapes. *PNAS*, 111, 6576–6581.

Rempe, D. M., & Dietrich, W. E. (2018). Direct observations of rock moisture, a hidden component of the hydrologic cycle. *PNAS*, 115, 2664–2669. https://doi.org/10.1073/pnas.1800141115

Rich, E. I. (1971). Geologic map of the Wilbur Springs quadrangle, Colusa and Lake counties, California (Tech. Rep.).

Riebe, C. S., Hahm, W. J., & Brantley, S. L. (2017). Controls on deep critical zone architecture: A historical review and four testable hypotheses: Four testable hypotheses about the Deep Critical Zone. *Earth Surface Processes and Landforms*, 42(1), 128–156. https://doi.org/10.1002/esp.4052

Sanders, M., Nelson, M. D., Bryk, A. B., Huang, M.-H., Fauria, K., & Dietrich, W. E. (2019). The role of small shallow landslides in landscape evolution as revealed by high resolution differential lidar surveys and field mapping. In AGU fall meeting 2019. AGU.

Schmidt, L., & Rempe, D. (2020). Quantifying dynamic water storage in unsaturated bedrock with borehole nuclear magnetic resonance. *Geophysical Research Letters*, 47(22). https://doi.org/10.1029/2020GL089600

Slim, M., Perron, J. T., Martel, S. J., & Singha, K. (2014). Topographic stress and rock fracture: A two-dimensional numerical model for arbitrary topography and preliminary comparison with borehole observations. *ESPL*, 40, 512–529. doi: 10.1002/esp.3646.

St Clair, J., Moon, S., Holbrook, W. S., Perron, J. T., Riebe, C. S., Martel, S. J., & d. Richter, D. (2015). Geophysical imaging reveals topographic stress control of bedrock weathering. *Science*, 350(6260), 534–538. https://doi.org/10.1126/science.aab2210

Sullivan., P. L., Billings, S. A., Hirmas, D., Li, L., Zhang, X., Ziegler, S., Murenbeeld, K., et al. (2022). Embracing the dynamic nature of soil structure: A paradigm illuminating the role of life in critical zones of the Anthropocene. *Earth Science Reviews*, 225. https://doi.org/10.1016/j.earscirev.2021.103873

Wang, W., Nyblade, A. A., Mount, G., Moon, S., Chen, P., Accardo, N., Gu., X, et al. (2021). 3D seismic anatomy of a watershed reveals climate-topography coupling that drives water flowpaths and bedrock weathering. *Journal of Geophysical Research: Earth Surface*, 126. https://doi.org/10.1029/2021JF006281

West, N., Kirby, E., Nyblade, A. A., & Brantley, S. L. (2019). Climate preconditions the critical zone: elucidating the role of subsurface fractures in the evolution of asymmetric topography. *ESPL*, 513, 197–205.

Xu, X., Sandwell, D. T., Klein, E., & Bock, Y. (2021). Integrated Sentinel-1 InSAR and GNSS time-series along the San Andreas fault system. *Journal of Geophysical Research: Solid Earth*, 126. https://doi.org/10.1029/2021JB022579

Zeng, Y., Petersen, M. D., & Shen, Z.-K. (2018). Earthquake potential in California-Nevada implied by correlation of strain rate and seismicity. *Geophysical Research Letters*, 45, 1778-1785. https://doi.org/10.1002/2017GL075967

AGU PUBLICATIONS

JGR: Earth Surface

Supporting Information for

Mapping variations in bedrock weathering with slope aspect under a sedimentary ridge-valley system using near-surface geophysics and drilling

Berit M. Hudson Rasmussen[1], Mong-Han Huang[1], W. Jesse Hahm[2], Daniella M. Rempe[3], David Dralle[4], and Mariel D. Nelson[3]

[1]Department of Geology, University of Maryland, College Park, MD, USA,

[2]Department of Geography, Simon Fraser University, Burnaby, BC, Canada,

[3]Department of Geosciences, Jackson School of Geosciences, The University of Texas at Austin, Austin, TX, USA,

[4]Pacific Southwest Research Station, United States Forest Service, Albany, CA, US

Contents of this file

Figures S1 to S14
Tables S1 to S2

Introduction

Text S1 describes seismic velocity results not shown in the main text.
Figure S1 shows seismic line 2 results parallel to the bedding.
Figure S2 shows seismic line 3 results perpendicular to the bedding.
Figure S3 compares velocity profile with seismic velocity surveyed parallel or perpendicular to the bedding.
Figure S4 shows seismic lines 4 and 5 result along two maximum hillslope descend profiles.
Figure S5 shows seismic line 9 results perpendicular the bedding and across the main ridge.
Figure S6 shows seismic lines 10 and 11 results along the MH2 channel.
Figure S7 compares the critical zone structure for north- and south-facing hillslopes for lines 4 and 5, respectively.
Figure S8 compares weathering thickness on north- and south-facing hillslopes for line 6.
Figure S9 compares weathering thickness between north- and south-facing hillslopes of MH2, MH3, MH7, and MH8 based on interface 3 property.
Figure S10 shows a 1D porosity model for MH3R (Line 7).

Figure S11 shows a 1D porosity model for MH2R (Line 7).

Figure S12 compares 1D velocity profiles between mean west- and east-facing hillslopes of lines 8 and 9.

Figure S13 shows an average porosity with depth for the MH7R ridgetop.

Figure S14 shows the topography of interface 3 along north or south facing hills.

Table S1 lists the model parameters used for the seismic inversion.

Table S2 lists the elastic modulii for minerals used in the rock physics model.

Supplementary Text S1 – Summary of seismic velocity models (lines 3, 4, 5, 9)

S1.1 MH7R Bedding-Perpendicular (Line 3)

The low-velocity material of the bedding-perpendicular profile (Line 3; **Figure S2**) is generally faster than material in the same depth range of the bedding-parallel profile (**Figures 4, S1**). CoV is < 20% almost everywhere above the deepest raypath, indicating consistency of velocity distribution between model ensembles (**Figure S2b**). The mean vertical gradient is lower than that of the bedding-parallel survey line, indicating a more gradual increase in velocity with depth (**Figure S2c**). The highest gradients (> 500 m/s/m) are located below the channel. 1D velocity at the intersection point with bedding-parallel Line 1 indicates an overall similar profile, however Line 3 is slightly faster above a 6m depth (**Figure S3**). Similar to Lines 1 and 2, we do not reach high-velocity material below the MH7R ridgetop in this survey line.

S1.2 MH8 North-Facing Slope (Line 4) and MH7 South-Facing Slope (Line 5)

Lines 4 (north-facing) and 5 (south-facing) are traced roughly perpendicular to the topographic contour lines to capture the steepest descent of the hillslope. Both survey lines show upslope-thickening weathering with a 30 m-thick weathered zone at the ridgetop (**Figure S4a,c**). The two slopes appear to have a similar thickness of low-velocity material, although the south-facing slope has considerably thinner mid-velocity (1000-3000 m/s) material. Velocity appears to increase more gradually below the north-facing slope and increases more rapidly on the south-facing slope. There is Vp > 4000 m/s visible more than halfway up the south-facing slope, faster than is resolved in Line 1. Line 5 also resolves deeper (~35 m) below the MH7R ridge than Line 1 (only ~15 m), possibly due to a longer maximum source-receiver distance for Lines 4 and 5.

S1.3 MH2R Perpendicular (Line 9)

Three boreholes at MH2R are within 10 m of Line 9: MH3-W5, MH3-W7, and MH3-W8. CoV is high (> 50%) below the ridgetop, but along the slopes, we can resolve up to 30-40 m depth. Velocity gradient is once again highest at the channels and is generally < 200 m/s/m elsewhere (**Figure S5a**). Similar to Line 8, velocity appears mostly sub-parallel to the topography (**Figure 7**). The low-velocity layer is uniformly 6-8 m thick along the east-facing slope of the MH2R perpendicular profile, with the exception of the eastern channel where it is < 3 m thick. The middle-velocity layer is more variable, increasing to > 10 m thick where the slope angle is most gradual, and thinning where the hillslope is steepest. The mid-velocity layer is nearly absent at the eastern channel, but it is still several meters thick at the western channel.

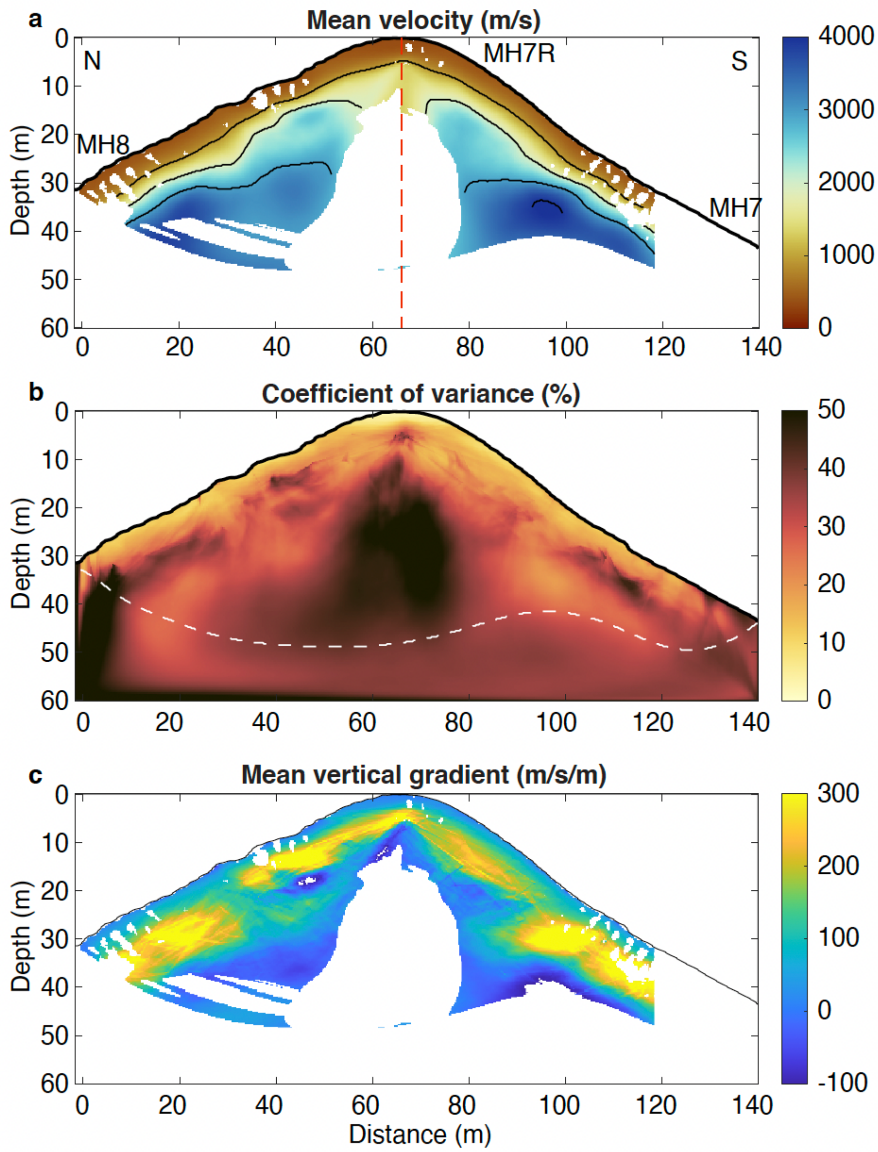

Figure S1. Results of Line 2 (**a-c**) inversion using THB rj-MCMC (Huang et al., 2021). (**a**) Mean velocity model with contour lines at 1000, 2000, 3000, and 4000 m/s. The model is masked out where no geophones are present (edges of survey), below the deepest raypath, and where coefficient of variation (CoV; standard deviation/mean velocity x 100) > 30%. The vertical dashed line highlights the locations of borehole MH7-W1. The same line also indicates the intersection point of Line 2 with Line 1 (see Figure 1b). (**b**) Percent CoV with the deepest raypath as the white dashed line. (**c**) Mean vertical velocity gradient (m/s/m).

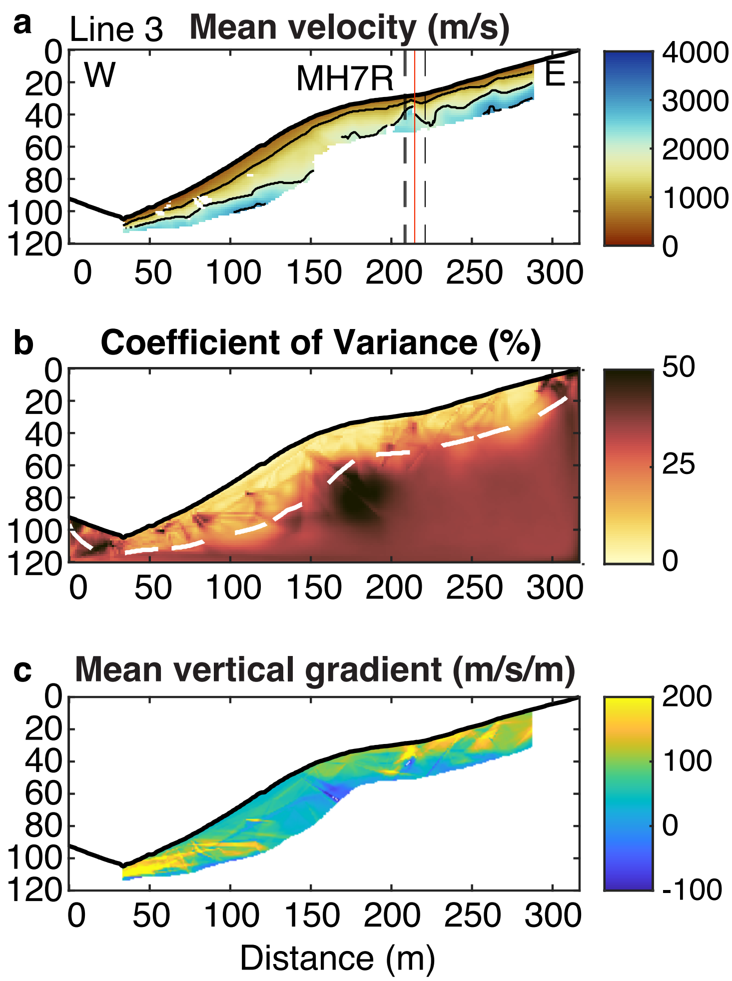

Figure S2. Results of Line 3 (**a-c**) inversion using THB rj-MCMC (Huang et al., 2021). (**a**) Mean velocity model with contour lines at 1000, 2000, 3000, and 4000 m/s. The model is masked out where no geophones are present (edges of survey), below the deepest raypath, and where coefficient of variation CoV > 30%. Vertical dashed lines highlight the locations of boreholes within 10 m of the survey line. From west to east, these include boreholes MH7-W2, MH7-W3, and MH7-W1. The orange vertical line indicates the intersection point of Lines 1 and 3. (**b**) Percent CoV with the deepest raypath as the white dashed line. (**c**) Mean vertical velocity gradient (m/s/m).

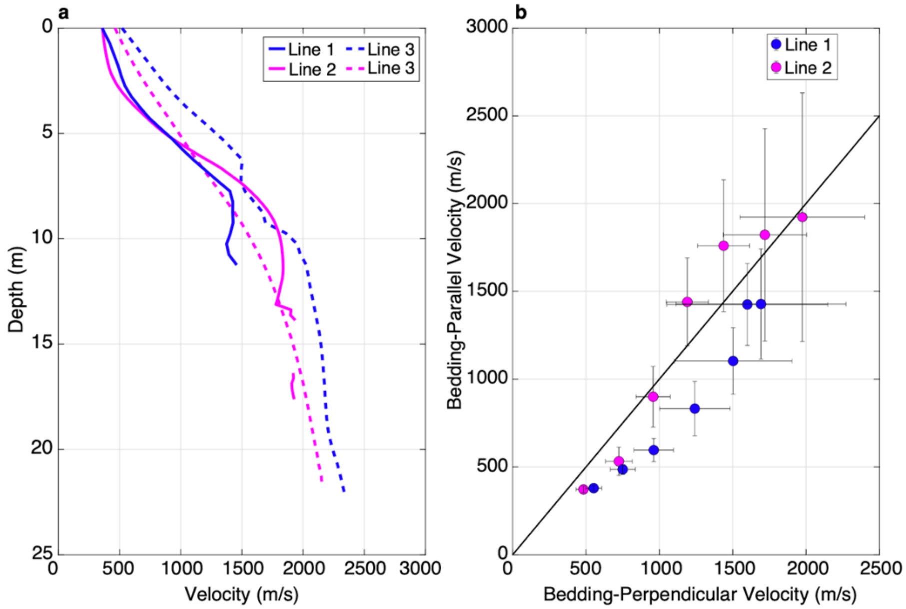

Figure S3. Velocity with depth at the intersection points of bedding-parallel and bedding-perpendicular survey lines for MH7R. (**a**) Solid and dashed lines show the velocity for bedding-parallel and bedding-perpendicular lines, respectively. (**b**) Bedding-perpendicular velocity vs bedding-parallel velocity. Blue circles represent the velocities at the intersection of Lines 1 and 3, and pink circles represent the velocities at the intersection of Lines 2 and 3.

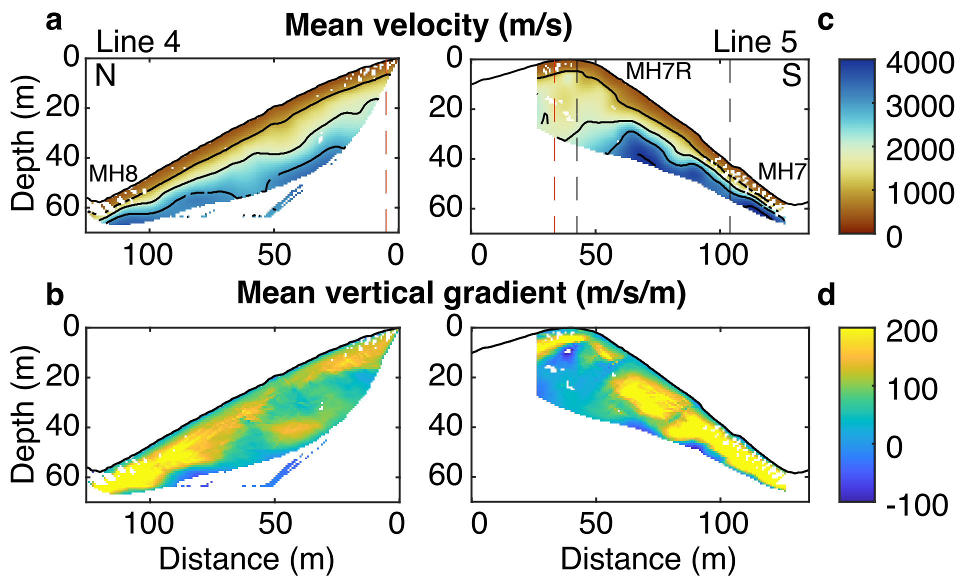

Figure S4. Results of Line 4 (**a-b**) and Line 5 (**c-d**) inversions. (**a,c**) Mean velocity model with contour lines at 1000, 2000, 3000, and 4000 m/s. The model is masked out below the deepest raypath and where CoV > 30%. Black dashed lines highlight the locations of boreholes within 10 m of the survey line (borehole MH7-W2 for Line 4; boreholes MH7-W2, MH7-W3, and MH7-W4 for Line 5). Lines 4 and 5 intersect at the MH7-W2 borehole (red dashed line). (**b,d**) Mean vertical velocity gradient (m/s/m).

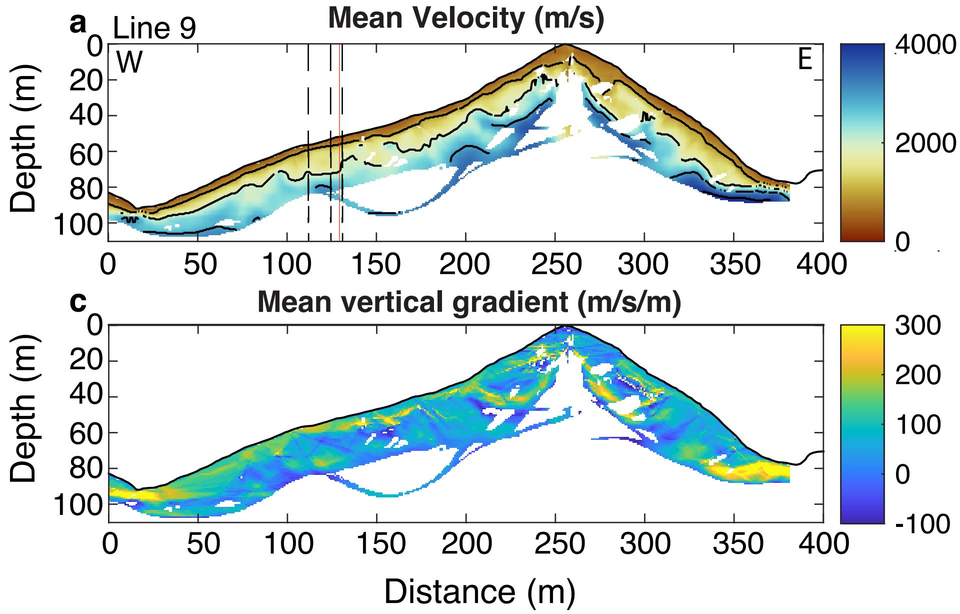

Figure S5. Results of Line 9 inversion. (**a**) Mean velocity model with contour lines at 1000, 2000, 3000, and 4000 m/s. The model is masked out below the deepest raypath and where CoV > 40%. Black dashed lines highlight the locations of boreholes within 10 m of the survey line. From west to east, these include boreholes MH3-W8, MH3-W7, and MH3-W5. The orange vertical line indicates the intersection point with Line 7. (**b**) Mean vertical gradient (m/s/m). Note the gradient color scale ranges from -100 to 300 m/s/m.

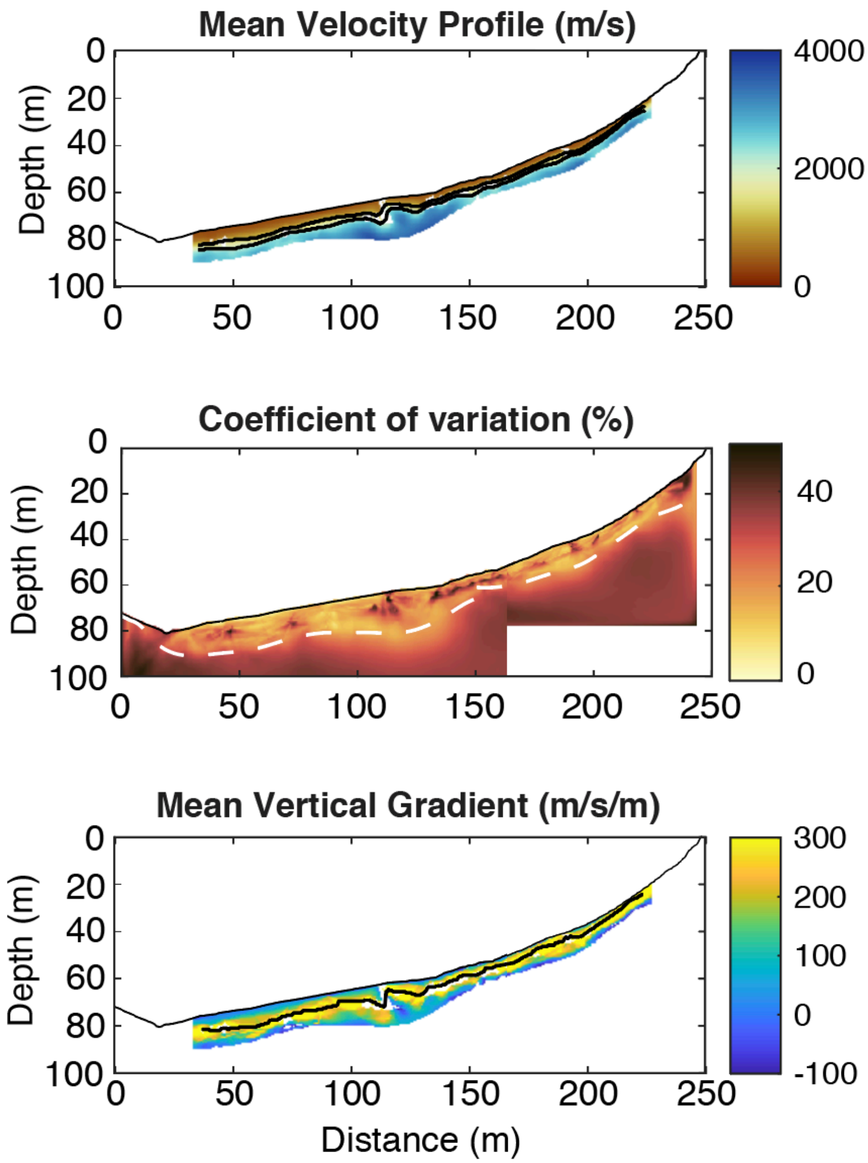

Figure S6. Results of Lines 10 and 11 (**a**-**c**) inversion using THB rj-MCMC (Huang et al., 2021). (**a**) Mean velocity model with contour lines at 1000, 2000, 3000, and 4000 m/s. The model is masked out where no geophones are present (edges of survey), below the deepest raypath, and where CoV > 30%. (**b**) Percent CoV with the deepest raypath as the white dashed line. (**c**) Mean vertical velocity gradient (m/s/m).

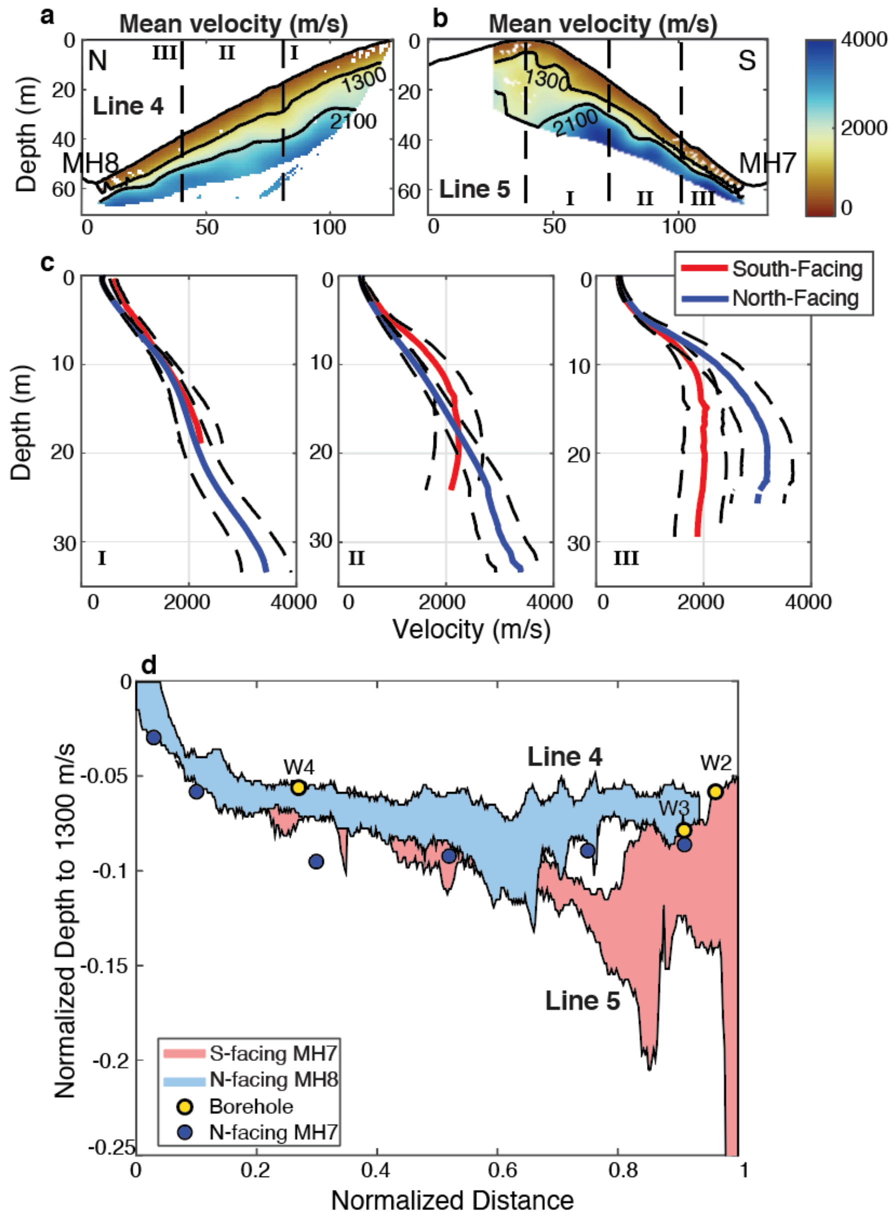

Figure S7. Comparison of Interface 2 depth for north- and south-facing hillslopes of Lines 4 and 5 (steepest descent of the slope). Mean velocity profiles for Lines 4 and 5 are shown in (**a**) and (**b**), respectively. Contour lines are at the approximate velocities of the Interface 2 (1284 m/s) and Interface 3 (1972 m/s) transitions. Roman numerals indicate three sections of the hillslopes used in (**c**). (**c**) shows 1D velocity profiles for three sections of the hillslope for north-facing (blue) and south-facing (red) slopes. Dashed black lines indicate 1 standard deviation. (**d**) Normalized depth to Interface 2 (1284 m/s contour) with normalized hillslope length. Zero is the channel and one is the ridgetop position. Blue circles represent points where Line 1 intersects a steepest descent transect, since we have no steepest descent survey line for MH7N. Yellow circles represent normalized Interface 2 depth in boreholes MH7-W2, MH7-W3, and MH7-W4.

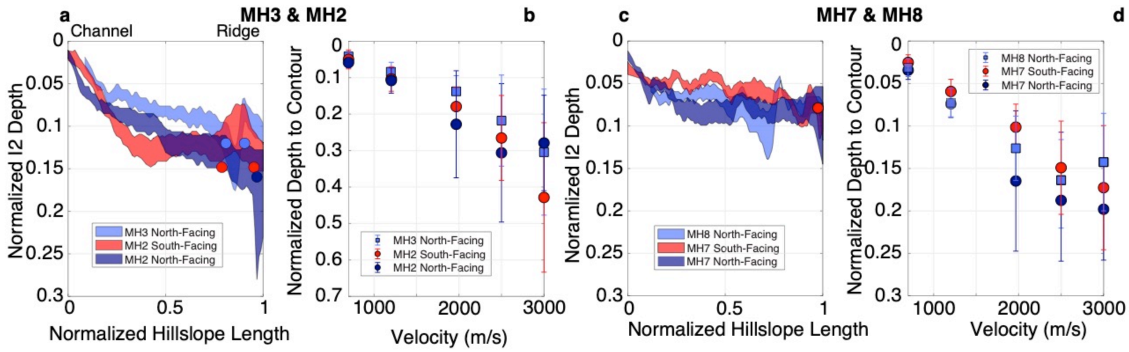

Figure S8. Comparison of weathering thickness on north- versus south-facing hillslopes for Line 6 (**ab**), and Line 1 (**cd**). Depth to Interface 2 (I2; saprolite-weathered bedrock) with normalized hillslope length (**a,c**) is shown based on the I2 velocity range (1284 ± 203 m/s velocity contours). Average depths to various velocity contours are shown normalized to hillslope length in (**b, d**), including the average Interface 2 velocity contour (1284 m/s) and average Interface 3 velocity contour (1973 m/s).

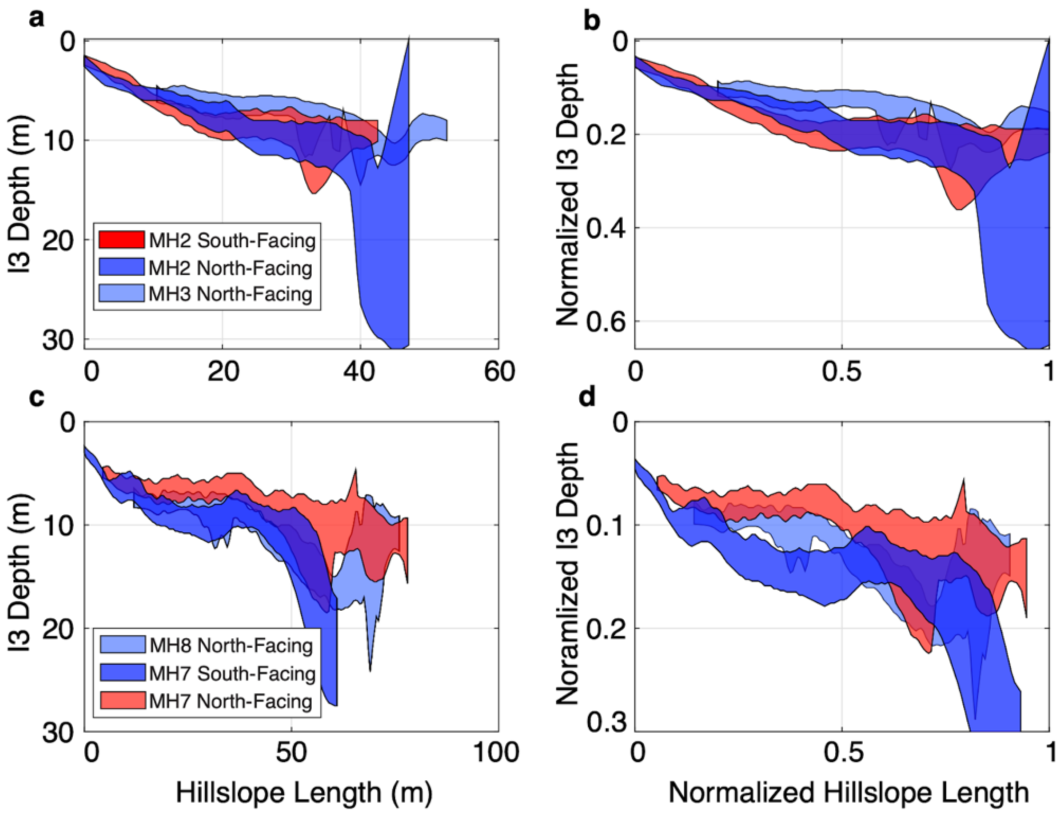

Figure S9. Comparison of weathering thickness on north- versus south-facing hillslopes for Line 6 (**a-b**), and Line 1 (**c-d**). Depth to Interface 3 (I3; weathered-unweathered bedrock transition) with hillslope length is shown based on the 1972 m/s velocity contour. (**b,d**) represent the same as (**a,c**), but hillslope length and depth to I3 are normalized by the hillslope length.

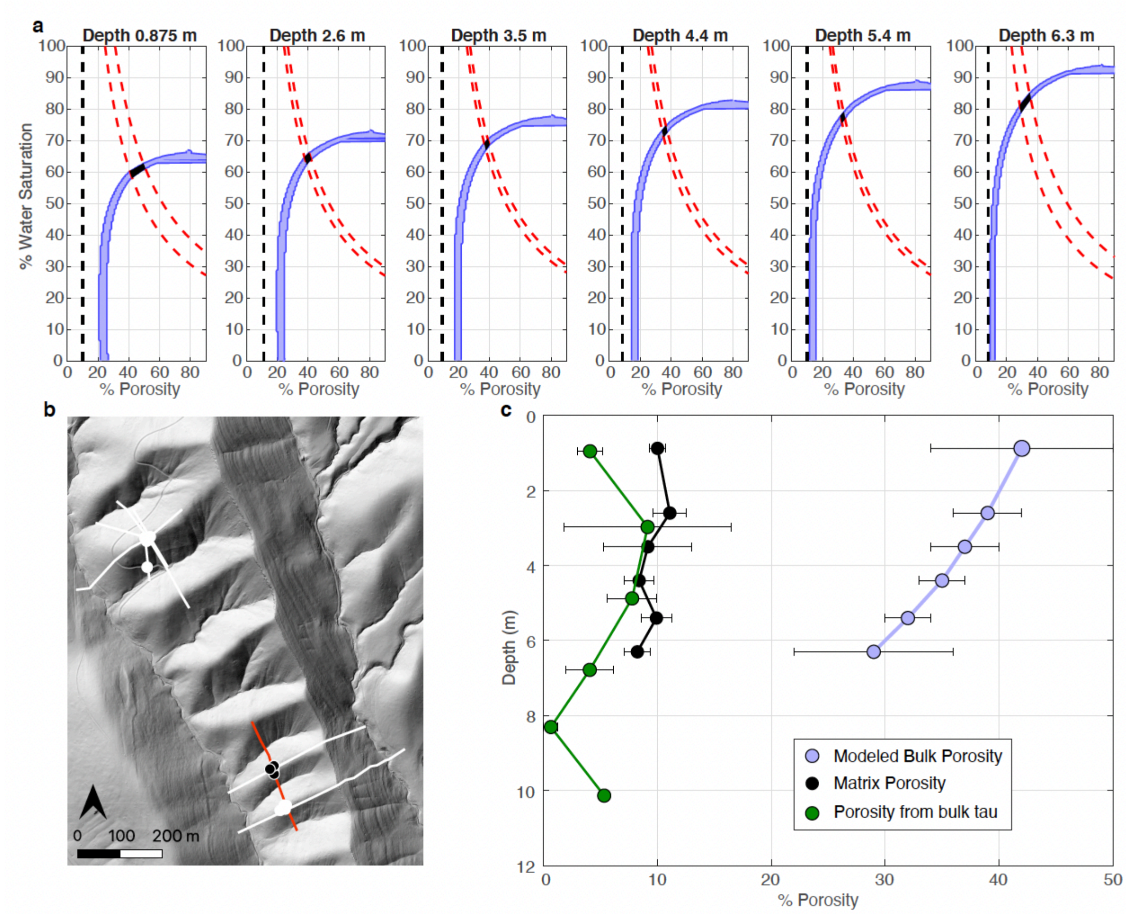

Figure S10. 1D rock physics model at MH3R (Line 7). (**a**) Tradeoff between saturation and porosity at MH3R at different depths. The thickness of the purple bar represents variation within a given mineral composition. The dashed black line is the measured matrix porosity from Pedrazas et al. (2021). The dashed red line indicates a tradeoff between porosity and saturation based on the volumetric water content measurement (Hahm et al., 2022). The black polygon indicates the inferred porosity and saturation based on both seismic refraction and the water content measurements. (**b**) Location of Line 7 (red line) and the boreholes used to measure volumetric water content (black circles). (**c**) Porosity with depth from the rock physics model (purple), the measured matrix porosity (black) and from bulk τ (green), assuming no contribution to porosity from volumetric strain.

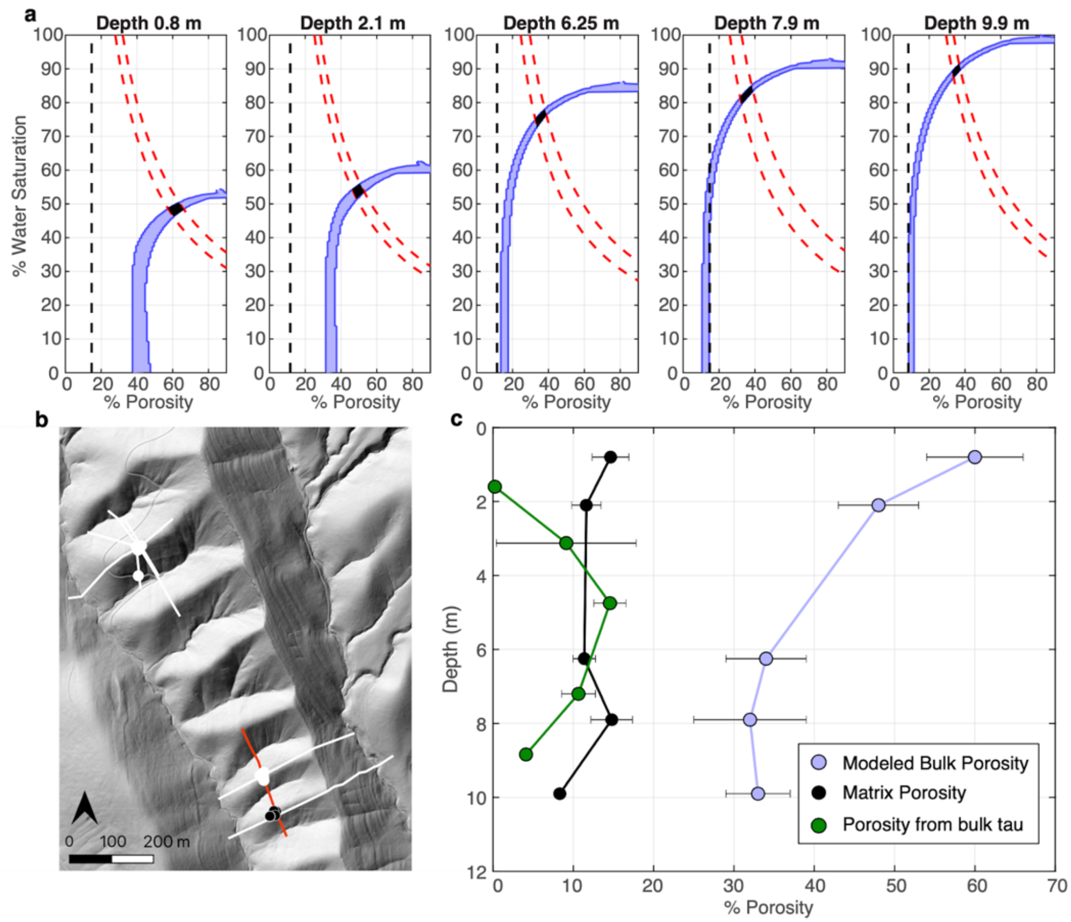

Figure S11. 1D rock physics model at MH2R (Line 7). (**a**) Tradeoff between saturation and porosity at MH2R at different depths. The thickness of the purple bar represents variation within a given mineral composition. The dashed black line is the measured matrix porosity from Pedrazas et al. (2021). The dashed blue line indicates a tradeoff between porosity and saturation based on the volumetric water content measurement (Hahm et al., 2022). The black polygon indicates the inferred porosity and saturation based on both seismic refraction and the water content measurements. (**b**) Location of Line 7 (red line) and the boreholes used to measure volumetric water content (black circles). (**c**) Porosity with depth from the rock physics model (purple), the measured matrix porosity (black) and from bulk τ (green), assuming no contribution to porosity from volumetric strain.

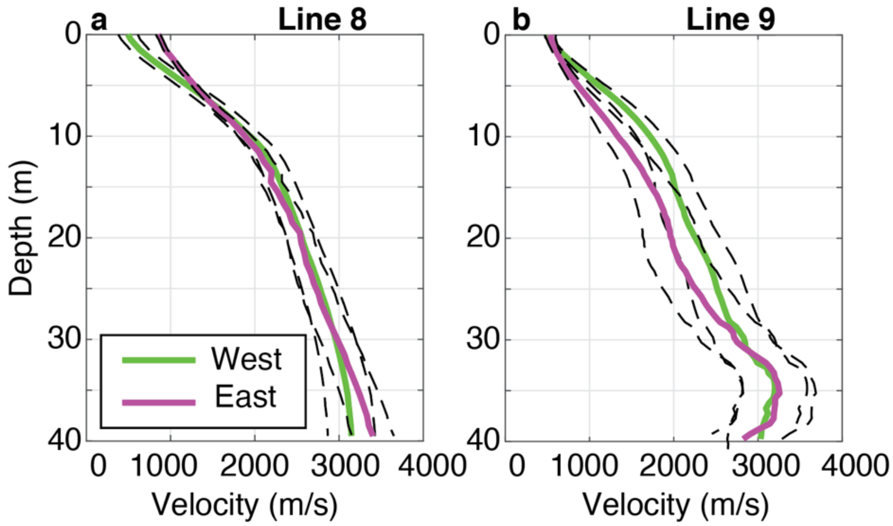

Figure S12. Average 1D velocity profile across the entire west-facing (green) and east-facing (pink) slopes for Lines 8 (**a**) and 9 (**b**). Dashed black lines represent 1 standard deviation.

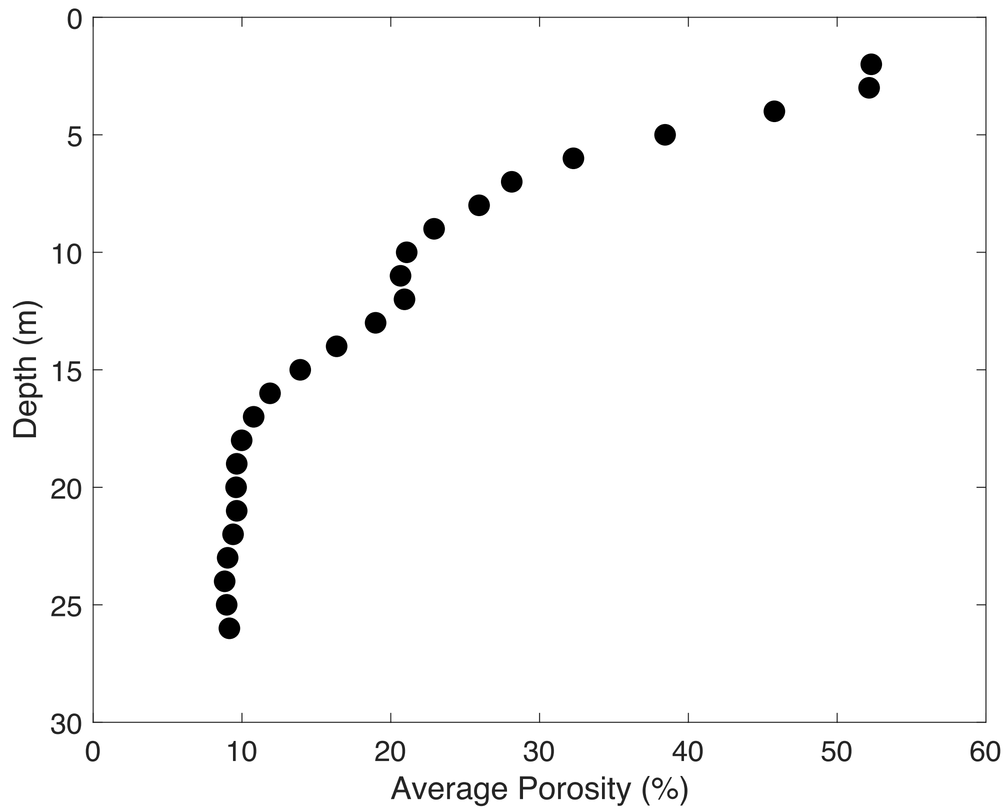

Figure S13. Average porosity with depth for the MH7R ridgetop (Line 1). Porosity values were averaged across 180-200 m horizontal distance of the 2D model (**Figure 12**).

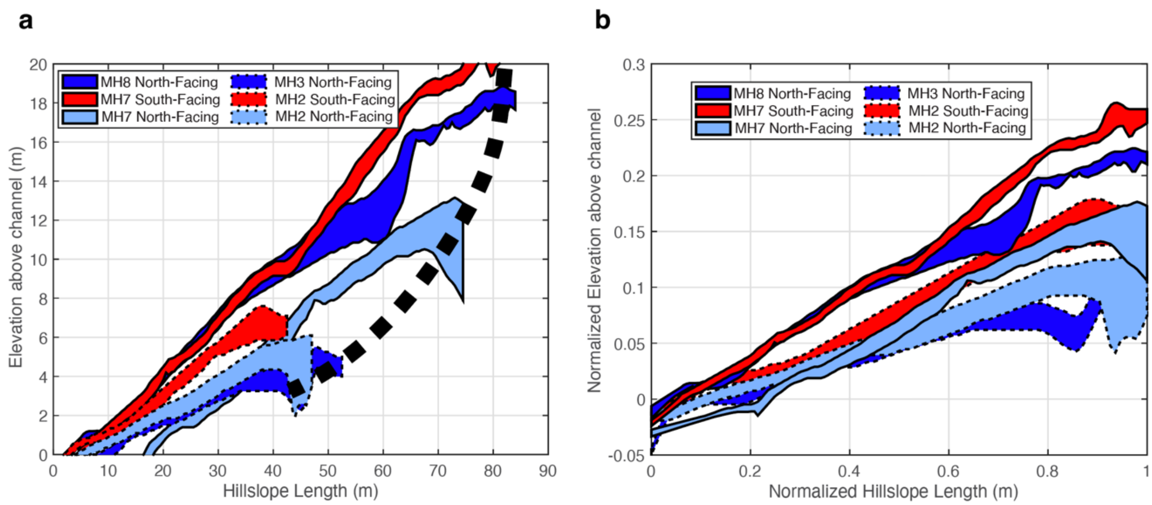

Figure S14. (a) Topography of interface 3 with hillslope length. The 6 different profiles are north (blue) and south (red) facing hills from seismic lines 1 and 7. The thick black dash curves suggests a non-linear scaling relationship between hillslope length and elevation of bedrock right below ridgetops. **(b)** Same as **a** but the hillslope length of each profile is normalized. Note there is no consistent pattern between different profiles.

Table S1. List of model parameters used in different seismic refraction survey lines.

Survey Line	Date	Geophone Number, Spacing (m)	Grid Size (m)	Markov Chains	Iterations	Mean misfit (ms)	Std. Dev. of Misfit (ms)	Noise Hyper-parameter (ms)
Line 1	08/2019	24, 3	0.5	10	1.5×10^6	1.23	1.6	1.47
Line 2	08/2021	48, 3	0.25	100	1.2×10^6	0.84	1.09	1.09
Line 3	08/2019	24, 3	0.5	15	1.0×10^6	1.67	2.13	2.00
Line 4	08/2021	48, 3	0.25	100	1.5×10^6	1.30	1.70	1.23
Line 5	08/2021	48, 2.5	0.25	100	1.5×10^6	1.16	1.47	1.16
Line 6	08/2021	48, 2	0.25	18	1.3×10^6	0.89	1.17	1.05
Line 7	12/2019	24, 3	0.5	15	1.2×10^6	1.14	1.64	1.62
Line 8	08/2021	48, 5	1	10	0.7×10^6	1.75	2.25	2.23
Line 9	01/2018	72, 2	0.5	15	2.9×10^6	1.35	1.85	1.5-1.8
Line 10/11	12/2019	24, 3	0.5	10	0.8×10^6/ 1.0×10^6	1.29/0.96	1.78/1.23	1.70/1.20

Table S2. Elastic modulii for minerals used in rock physics model (Mavko et al., 2009; Gu et al., 2020s).

Mineral	Bulk Modulus (Pa)	Shear Modulus (Pa)
Quartz	37×10^9	44×10^9
Feldspar	37.5×10^9	15×10^9
Illite	52.3×10^9	31.7×10^9